^{238}U, ^{235}U and ^{234}U in seawater and deep-sea corals: A high-precision reappraisal

Michael A. Kipp [a,*], Haoyu Li [a], Michael J. Ellwood [c], Seth G. John [d], Rob Middag [e], Jess F. Adkins [b], François L.H. Tissot [a]

[a] *The Isotoparium, Division of Geological and Planetary Sciences, California Institute of Technology, Pasadena, CA, USA*
[b] *Division of Geological and Planetary Sciences, California Institute of Technology, Pasadena, CA, USA*
[c] *Research School of Earth Sciences, Australian National University, Canberra, ACT, Australia*
[d] *Department of Earth Sciences, University of Southern California, Los Angeles, CA, USA*
[e] *Department of Ocean Systems, Royal Netherlands Institute for Sea Research (NIOZ), Texel, Netherlands*

ARTICLE INFO

ABSTRACT

Uranium isotope ratios are widely utilized in paleoceanography. The ^{238}U/^{235}U ratio (expressed as δ^{238}U) is leveraged as a proxy for the areal extent of anoxic seafloor, and the ^{234}U/^{238}U ratio (expressed as δ^{234}U$_{sec}$) tracks riverine and estuarine inputs to the ocean, in addition to featuring prominently in U-series geochronology. Both of these ratios are thought to be recorded by biological carbonates precipitating from seawater, with corals serving as one of the most commonly-used archives of seawater U isotope ratios in the past. The utility of the U isotope proxy in biological carbonate archives relies not only on this faithful archiving of ambient seawater signatures, but also on the homogeneity of the seawater U isotope composition, which enables samples to be leveraged as proxy for the entire ocean.

Here we revisit the foundational assumption of homogeneity of the marine U reservoir, and the capacity of deep-sea corals to record the U isotopic composition of ambient seawater. We begin by evaluating the analytical limits of precision and accuracy achievable for both δ^{238}U and δ^{234}U$_{sec}$ analysis by MC-ICP-MS. We then report data for 45 seawater and 26 deep-sea coral samples from multiple sites around the world. We find subtle δ^{238}U and δ^{234}U$_{sec}$ heterogeneity that correlates with U concentrations, which allows us to calculate new salinity-normalized global mean seawater values for δ^{238}U (−0.379 ± 0.023 ‰) and δ^{234}U$_{sec}$ (+145.55 ± 0.28 ‰). At each site, biological carbonates act as precise archives of the seawater δ^{238}U value. The same is true for δ^{234}U$_{sec}$, with a few exceptions where samples appear to show vital effects that cause intra-sample ^{234}U/^{238}U re-partitioning. In sum, these observations support deep-sea corals as a robust archive of seawater U isotope ratios, but highlight the importance of utilizing multiple sample sites and replicate analyses to overcome coral vital effects (for δ^{234}U$_{sec}$) and subtle marine U isotopic heterogeneity.

1. Introduction

Uranium (U) has been an important oceanographic tracer for over half a century (Veeh, 1967; Ku et al., 1977; Klinkhammer and Palmer, 1991). In early work, much of this utility was derived from ^{238}U decay into ^{234}U and ^{230}Th, rendering U one of the best time-keepers for processes occurring in the recent geologic past (Edwards et al., 1987b; Cheng et al., 2000b, 2013). More recently, the recognition of natural fractionation of ^{238}U/^{235}U (Stirling et al., 2007; Weyer et al., 2008) has enabled redox-driven U isotope

fractionation to be leveraged as a proxy for past ocean anoxia (e.g., Lau et al., 2019). Importantly, in both geochronology and paleo-redox applications, the conservative behavior of U in seawater (Ku et al., 1977; Owens et al., 2011) – in other words, its long mean residence time (~400 kyr) in the ocean – is leveraged to draw inferences about global processes. This allows samples from a single locality to, in theory, inform our understanding of the ocean as a whole, which gives the U proxy enormous utility in paleoceanography.

While the U proxy – both for geochronology and paleo-redox studies – has been calibrated in modern seawater and biological archives (Chen et al., 1986; Cheng et al., 2000a; Chen et al., 2018b; Tissot and Dauphas, 2015; Tissot et al., 2018), no study

---

* Corresponding author.
  E-mail address: mkipp@caltech.edu (M.A. Kipp).

has thoroughly revisited these calibrations with high-precision methods for U isotope analysis. Thus, while the U proxy has been successfully used to track episodes of widespread marine anoxia in the distant past (e.g., Clarkson et al., 2018; Zhang et al., 2018), it has to-date not been utilized with sufficient precision to resolve subtle redox changes in more recent geologic history, i.e., the Cenozoic (Wang et al., 2016; Gothmann et al., 2019; Clarkson et al., 2021). Such applications could be particularly useful in the study of climate evolution in the Quaternary, as high-temporal-resolution biological archives (e.g., deep-sea corals; Robinson et al., 2007) should in theory enable such records to be generated. Indeed, such archives have been used to evaluate subtle $^{234}U/^{238}U$ trends during the last deglaciation (Chen et al., 2016; Chutcharavan et al., 2018). However, the recognition of basin-scale heterogeneity in Quaternary U isotope records (Chen et al., 2016) raises questions about the ability of the U proxy to serve as a global tracer during such transient perturbations. Before attempting reconstructions of seawater U isotope ratios during these perturbations, it is therefore necessary to more precisely evaluate (i) the homogeneity of U isotope ratios in modern seawater, and (ii) the extent to which biological archives record the ambient U isotope composition.

Here, we present new high-precision $^{238}U/^{235}U$ and $^{234}U/^{238}U$ data from 45 seawater and 26 modern deep-sea corals from multiple localities around the world. Our data show that these corals record seawater U isotope ratios extremely well within analytical uncertainty. However, we also observe variable $^{238}U/^{235}U$ – and to a lesser extent $^{234}U/^{238}U$ – along depth profiles. Furthermore, there appear to be subtle differences in both $^{238}U/^{235}U$ and $^{234}U/^{238}U$ across ocean basins. These findings collectively support the utility of deep-sea corals as archives of ambient seawater U isotope ratios in the past, but highlight the importance of utilizing multiple sample sites, as even in the modern ocean there is observable heterogeneity that could influence paleo-proxy interpretations.

2. Materials

2.1. Deep-sea corals

2.1.1. Background

Marine carbonates are widely utilized as archives of the seawater U isotope composition, as they are known to precipitate from seawater with little to no U isotopic fractionation (Weyer et al., 2008; Chen et al., 2018b; Tissot et al., 2018). While carbonate sediments are abundant in the geologic record, and have been targeted as archives of paleo-seawater $^{238}U/^{235}U$ ratios (e.g., Clarkson et al., 2018; Zhang et al., 2018), they are subject to dissolution and recrystallization reactions through early and late diagenesis. These reactions can both add and remove carbonate-hosted U, thereby altering U isotope signatures and causing bulk carbonate sediments to no longer faithfully record the seawater U isotope composition at the time of deposition (Romaniello et al., 2013; Chen et al., 2018a; Tissot et al., 2018).

Non-sedimentary carbonates (e.g., discrete fossils, such as corals) provide a potential solution to this problem. If U isotopes are measured in discrete biological carbonate phases, the often ambiguous and complicated diagenetic history of sedimentary carbonate can potentially be circumvented (Chen et al., 2018b; Tissot et al., 2018; Livermore et al., 2020). While such fossil archives are only present for more recent intervals of Earth history, they can provide important records of recent changes in ocean chemistry.

Among the best-studied biological archives for Quaternary paleoceanography are deep-sea corals. Deep-sea corals grow on hardground surfaces (e.g., seamounts) at hundreds to thousands of meters depth. These corals precipitate carbonate skeletons, and in doing so, record many aspects of ambient seawater chemistry (Adkins et al., 2003; Gagnon et al., 2007; S. Chen et al., 2021). Prior work has shown that shallow-water scleractinian ("stony") corals record seawater $^{238}U/^{235}U$ ratios (Chen et al., 2018b; Tissot et al., 2018); prior work has also shown that deep-sea scleractinian corals can record seawater $^{234}U/^{238}U$ ratios (Robinson et al., 2006). Here we specifically targeted deep-sea scleractinian corals of the taxon *Desmophyllum dianthus* (formerly *D. cristagalli*), which has been the focus of many paleoceanographic studies (e.g., Robinson et al., 2005; Hines et al., 2015; Wang et al., 2017).

Individual *D. dianthus* corals have a lifespan of decades, while populations of *D. dianthus* corals can persist in a habitat for millennia (Thiagarajan et al., 2013). This gives *D. dianthus* considerable utility as an archive of Quaternary seawater chemistry. Most work targets septa – plate-like structures radially oriented about the body axis (Fig. 1) – for geochemical analysis (e.g., Adkins et al., 2003; Gagnon et al., 2007; Robinson et al., 2005; Hines et al., 2015; Wang et al., 2017; S. Chen et al., 2021). While fine-scale features within individual septa can be probed to study vital effects and/or short time-series perturbations, here we homogenized entire septa to provide large samples for precise U isotope analysis.
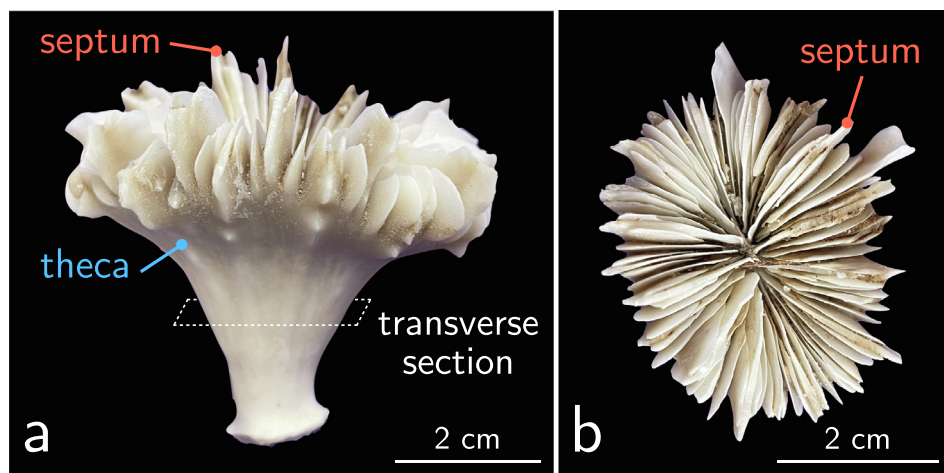
Fig. 1. Anatomy of a *D. dianthus* coral shown looking (a) parallel to transverse plane and (b) perpendicular to transverse plane. The modern specimen pictured was collected during the TN228 cruise (Section 2.1). The two main portions of the coral skeleton, the septa and theca, are labeled accordingly. For analysis, a single septum was removed from each coral and homogenized into a fine powder.

2.1.2. Coral samples utilized in this study

D. dianthus specimens were obtained from the Smithsonian Museum of Natural History and from sampling on the Tasmanian seamounts during cruise TN-228 in 2008–2009 (Fig. 2). These corals were collected with organic material present and are thus considered modern. The samples span a range of depths, allowing us to determine whether the contributions of different water masses and biogeochemical processes create U isotopic variability.

2.2. Seawater

Seawater samples were obtained from GEOTRACES stations that were in close proximity to the deep-sea coral specimens described above. These include samples from GEOTRACES cruises GA03, GA02 and GP13 in the North Atlantic, South Atlantic and South Pacific, respectively (Fig. 2). Samples were collected following standard GEOTRACES trace-metal clean protocols and acidified with HNO_3 prior to storage and shipping (Schlitzer et al., 2018).

## 3. Methods

3.1. Sample preparation

All sample preparation and analyses were performed at the Isotoparium (Caltech). Prior to chemical processing, seawater samples (30–60 mL) were spiked with the IRMM-3636 ^{233}U-^{236}U double spike (Verbruggen et al., 2008) such that a 3 % U_{spike}/U_{sample} ratio was achieved (assuming a U concentration of 3.2 ng/g for seawater with a salinity of 35 psu; Owens et al., 2011). Samples were then dried down in acid-cleaned PFA beakers at 120–140 °C. Twice-distilled, concentrated HNO_3 was then added to the residual salts, and beakers were capped and set on a hot plate overnight at 140 °C. Samples were dried the next day and this process was repeated (up to 4 times) until the solution remained clear after addition of the HNO_3 (indicating Cl had been removed, which would interfere with chemical purification). Samples were then diluted in 20 mL of 3 M HNO_3 in preparation for column chemistry.

Modern coral samples were first physically abraded to remove organic and mineral coatings (S. Chen et al., 2021). Whole coral septa were then sonicated in Milli-Q H_2O to remove detritus, dried, and powdered in an agate mortar and pestle. Powder aliquots (40–200 mg) were dissolved in ~3.5 M (20 % v/v) trace-metal grade acetic acid (Fisher Scientific) in pre-cleaned centrifuge tubes. Samples were then centrifuged and the supernatant was decanted into an acid-cleaned PFA beaker. The residues were resuspended in Milli-Q H_2O, centrifuged, and the supernatant again decanted into the PFA beaker. The resulting solutions were dried down completely at 140 °C, and reconstituted in 5 mL of 3 M HNO_3.

In parallel to the seawater and coral samples, we prepared and analyzed the USGS Columbia River Basalt (BCR-2) geostandard to monitor the long-term accuracy and precision of our methods. Sample powder (100–250 mg) was dissolved by consecutive acid attacks on hot plates using 4 mL of 3:1 $HF:HNO_3$, followed by 4 mL of 3:1 $HCl:HNO_3$ (aqua regia). These steps were then repeated. After the final dissolution step, 100–200 µL of $HClO_4$ was added to samples to dissolve residual fluorides. The $HClO_4$ was removed by heating at 165 °C for several hours, and the samples dried completely. The samples were then brought up in 5 mL of 3 M HNO_3.

Prior to spiking, the U content of coral and geostandard solutions was measured on an iCAP RQ ICP-MS (ThermoFisher). A 2–5 % aliquot was taken from the digest (in 3 M HNO_3) and diluted to 0.45 M HNO_3. Relative error of U concentration measurements was < 10 % in all runs as determined by replicate analyses of standard solutions. Coral and geostandard solutions were then spiked with IRMM-3636 to obtain a 3 % U_{spike}/U_{sample} ratio. Spiked samples were dried down and redissolved in 5 mL of 3 M HNO_3 for column chemistry.

Samples were purified using U/TEVA resin (Eichrom) following established protocols (e.g., Tissot and Dauphas, 2015). Following chemical purification, the U cut was dried down completely, 0.5 mL of 1:1 $HNO_3:H_2O_2$ were added, and beakers were capped and placed on a hot plate at 120 °C overnight to oxidize organic molecules released from the resin during column chemistry. Samples were dried down entirely the next day and brought up in 3 M
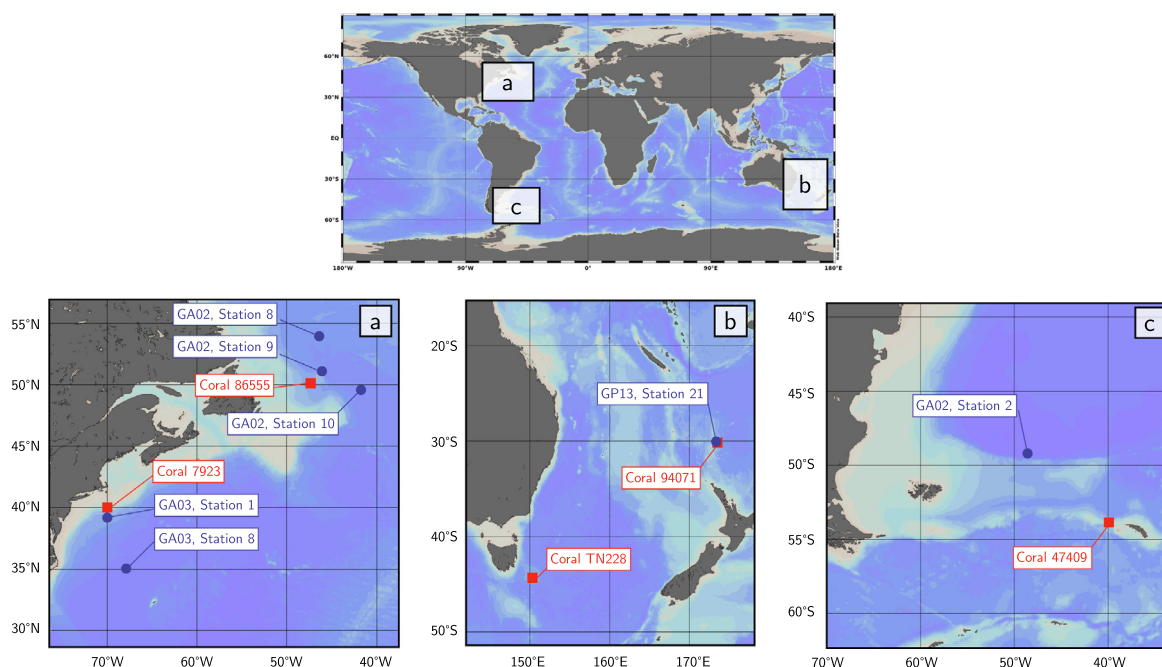
Fig. 2. Locations of seawater and coral samples. GEOTRACES stations marked with blue circles; coral sites marked with red squares. Maps were generated using Ocean Data View (Schlitzer et al., 2018). (For interpretation of the references to colour in this figure legend, the reader is referred to the web version of this article.)

HNO_3. Column chemistry was then repeated a second time to further remove matrix elements that have been shown to affect high-precision $^{234}U/^{238}U$ measurements (Tissot et al., 2018). The final U cuts were again treated with $HNO_3 + H_2O_2$ to degrade organics, dried and reconstituted in 15 M HNO_3, and ultimately diluted to 0.45 M HNO_3 for isotopic analysis.

3.2. U isotope analysis via MC-ICP-MS

All isotopic analyses were conducted on a Neptune*Plus* (ThermoFisher) multiple collector inductively coupled plasma mass spectrometer (MC-ICP-MS) at the Isotoparium. Solutions were introduced to the mass spectrometer in 0.45 M HNO_3 via an Aridus 3 (Teledyne CETAC) desolvating nebulizer (DSN) system. Measurements were conducted in static mode with ^{234}U as the center mass (Tissot and Dauphas, 2015). For most measurements, the ^{234}U signal was measured with a secondary electron multiplier (SEM), while all other masses were measured in Faraday (FAR) cups coupled to 10^{11} Ω resistors. The SEM-FAR yield (counts-*per*-second to volts) was determined daily by running our bracketing standard solution in a multi-line method that toggled the center cup between SEM and FAR mode (further details in **Section 4**).

Raw data were downloaded from the Neptune*Plus* and processed offline. The blank contribution was subtracted from each mass by monitoring on-peak zeros prior to each solution measurement. Instrumental mass bias was corrected via standard-sample bracketing and double spike deconvolution (Dodson, 1963; Tissot and Dauphas, 2015).

The $^{238}U/^{235}U$ ratios are reported as $\delta^{238}U$ values in units of permil relative to the U standard CRM-112a ($^{238}U/^{235}U$ = 137.837; Richter et al., 2010; also named SRM960 or NBL112-a; CRM-145 for the solution form):

$$\delta^{238}U = \left[\frac{^{238}U/\ ^{235}U_{sample}}{^{238}U/\ ^{235}U_{standard}} - 1 \right] \times 1000. \tag{1}$$

The $^{234}U/^{238}U$ ratios are expressed relative to secular equilibrium as:

$$\delta^{234}U_{sec} = \left[\frac{(^{234}U/\ ^{238}U)_{sample}}{(^{234}U/\ ^{238}U)_{S.E.}} - 1 \right] \times 1000, \tag{2}$$

where $(^{234}U/^{238}U)_{S.E.}$ is the atomic ratio at secular equilibrium and is equal to the ratio of the decay constants of ^{238}U and ^{234}U, $\lambda_{238}/\lambda_{234}$ = $(1.5513 \times 10^{-10})/(2.8220 \times 10^{-6})$ = 5.4970×10^{-5} (Cheng et al., 2013). Each sample was analyzed several times, and the analytical uncertainty is expressed as a 95 % confidence interval, calculated as $95\% CI = T \frac{\sigma}{\sqrt{n}}$ where T is Student's T value for the number of replicate analyses, σ is the standard deviation of replicate analyses, and n is the number of replicate analyses (typically between 8 and 21).

4. Precision and accuracy of isotopic analyses

As the goal of this study is to search for subtle isotopic trends that have escaped prior recognition, it is critical that we thoroughly demonstrate both the precision and accuracy of our analytical methods. In this section, we therefore walk through the relevant constraints on the precision and accuracy of our measurements, highlighting the ways these match or differ from prior work.

4.1. A brief history of U isotope analysis

Since the relative abundances of U isotopes were first reported at the percent-level nearly a century ago (Nier, 1939), the analytical precision of U isotopic analysis has improved by three orders of magnitude (Tissot and Ibañez-Mejia, 2021). The first leap occurred in the 1950′s-80′s, with the advent of thermal ionization mass spectrometry (TIMS) and digital mass spectrometers (Wasserburg et al., 1969), which made permil-scale precision routinely achievable for $\delta^{238}U$ measurements and ~ 5 ‰ precision feasible for $\delta^{234}U_{sec}$ (Chen et al., 1986). With the rise of MC-ICP-MS in the 1990's (Albarède et al., 2004; Halliday et al., 1998), precision of ≤ 0.1 ‰ became achievable for $\delta^{238}U$, leading to the first reports of natural $^{238}U/^{235}U$ variability (Stirling et al., 2007; Weyer et al., 2008). In the decade and a half since these pioneering reports, hundreds of studies have characterized $\delta^{238}U$ trends in natural materials, with some of the most recent studies reporting analytical precision of 10–30 ppm (0.01–0.03 ‰; Chen et al., 2018b; Tissot et al., 2018). With such precise measurements, it should in theory be possible to track subtle U isotope trends across physical and chemical gradients in the ocean. However, before doing so we must ensure that such precise analyses are indeed accurate within the reported precision. While one study (Tissot et al., 2019) has explored the limits of analytical precision for U-limited $\delta^{238}U$ analyses, no study has yet systematically evaluated the ultimate analytical limits of precision and accuracy achievable for both $\delta^{238}U$ and $\delta^{234}U_{sec}$ analysis by MC-ICP-MS. Below we walk through such an exercise before considering the results of our sample analyses.

4.2. Analytical precision

We begin by considering the precision of our analyses – i.e., how well can we reproduce the same measurement? To do this we follow work by Dauphas et al. (2009) and John and Adkins (2010) who undertook a similar exercise for Fe isotope analysis, and Tissot et al (2019) who undertook the same exercise for $\delta^{238}U$ measurements.

4.2.1. Internal error
We can start by calculating the maximum theoretically achievable precision for a single measurement (i.e., the "internal" precision). There are two contributions to analytical error that we must consider in this calculation: 1) electronic noise, called "Johnson noise" or "shot noise" ($\sigma_{Johnson}$) and 2) counting statistics ($\sigma_{counting}$). Johnson noise is a function of detector temperature (T), amplifier resistance (R), and measurement time (t), such that

$$\sigma_{Johnson} = \sqrt{\frac{4kTt}{e^2 R}} \tag{3}$$

where k is the Boltzmann constant (1.381×10^{-23} m^2 kg s^{-2} K^{-1}) and e is the elementary charge (1.602×10^{-19} C). The error from counting statistics is in contrast related only to the number of "counts" registered by a detector. In this case, the counts are ions hitting a Faraday cup or being counted in the SEM. John and Adkins (2010) define an operational variable, n_{eff}, calculated as

$$n_{eff} = \frac{n_a n_b}{n_a + n_b} \tag{4}$$

which can be used to describe the number of counts made by two detectors for a given isotope ratio measurement. Here, n_a and n_b refer to the number of atoms of the two isotopes of interest that are counted (i.e., ^{238}U and ^{235}U for $\delta^{238}U$, and ^{234}U and ^{238}U for $\delta^{234}U_{sec}$). For the SEM, this is equal to the measurement reported in units of counts-*per*-second (cps) multiplied by the integration time for a single measurement. For Faraday cups, the voltage registered can be related to counts assuming a cps/V value of 6.25×10^7 (small fluctuations in this value have a negligible effect in this

calculation, but will be considered in detail below). Using the n_{eff} notation, the error from counting statistics can be calculated as

$$\sigma_{counting} = \frac{1}{\sqrt{n_{eff}}} \qquad (5)$$

For a single measurement of known intensity and duration, we can then calculate $\sigma_{Johnson}$ and $\sigma_{counting}$ and cast them each as a function of n_{eff} (Fig. 3).

Under optimal analytical conditions, the analytical error on a single isotope ratio measurement will plot along the sum of the $\sigma_{Johnson}$ and $\sigma_{counting}$ lines. We find that our analyses – both of standard solutions and of actual samples that have been processed through our chemical purification protocol (Section 3.1) – indeed plot along the curve of maximum internal precision for $\delta^{238}U$ (Fig. 3a), with a third component ($\sigma_{unknown}$) calculated to represent remaining limitations on precision whose sources are not well-understood. The magnitude of this additional error that we observe here for U isotopes (0.014 ‰) is similar to that observed by John and Adkins (2010) for Fe isotopes (0.009 ‰). For $\delta^{234}U_{sec}$ measurements (Fig. 3b), there are two data populations: (1) those that plot at (or above) the sum of the $\sigma_{Johnson}$ and $\sigma_{counting}$ lines, for which ^{234}U was measured in a Faraday cup, and (2) those that plot along the $\sigma_{counting}$ line, for which ^{234}U was measured with the SEM (i.e., the amplifier noise is irrelevant).

Here we also briefly note the importance of matching the resistance of amplifiers during the measurement of two isotopes for precise determination of the isotopic ratio. For most of our analyses, we employed amplifiers with 10^{11} Ω resistors (hereafter "10^{11} Ω amplifier") for both the ^{238}U and ^{235}U signals. However, we tested the effect of instead utilizing a 10^{12} Ω amplifier for the ^{235}U signal, as this would reduce Johnson noise by a factor of $\sqrt{10}$. Since the ^{235}U signal is considerably smaller than the ^{238}U signal, the Johnson noise can contribute significantly to the analytical error and thus diminishing it would help improve the attainable precision of our analyses. When doing so, we see that internal error reaches a plateau that is worse than the maximum achievable precision (gold crosses, Fig. 3a). This is due to the longer recovery time of the 10^{12} Ω amplifier compared to that of the 10^{11} Ω amplifier

(Klaver et al., 2016). This effect could potentially be corrected by employing a dynamic time correction, or "tau" correction (Kimura et al., 2016; Craig et al., 2017), but we instead opted to utilize uniform amplifiers for all measurements and increase the voltage as much as possible to reduce the relative impact of Johnson noise on our internal precision. Due to the large dynamic range of U isotopic abundance ($^{238}U/^{235}U \sim 10^2$), this leaves us still in a realm where Johnson noise is a non-negligible source of error (Fig. 3a) while we are approaching the maximum voltage (50 V) for the ^{238}U signal on a 10^{11} Ω amplifier. Running at a $10\times$ higher concentration and employing a 10^{10} Ω amplifier for ^{238}U is one way around this limitation on maximal internal precision, because the decay time difference between 10^{10} and 10^{11} Ω resistors does not limit precision (as they are both much shorter than the 4.194 s measurement cycle). However, running such intense beams can lead to rapid degradation of the graphite liners of Faraday cups (Chakrabarti et al., 2021), so we also avoided this approach and ultimately opted to increase the number of analyses rather than measurement intensity.

We also note that despite achieving sub-optimal precision, the use of a 10^{12} Ω amplifier on the minor isotope still outperforms matched 10^{11} Ω amplifiers in the region of n_{eff} space where Johnson noise is the dominant source of error ($n_{eff} < 10^8$) (Fig. 3b). As this is the region of n_{eff} space for all $\delta^{234}U_{sec}$ measurements undertaken here, we utilized a 10^{12} Ω amplifier in all tests where ^{234}U was measured in a Faraday cup (Fig. 3b).

4.2.2. Intermediate and external error

Having demonstrated that each individual analysis is maximizing the attainable precision of the instrument, we can then consider the "intermediate" and "external" error; i.e., the error associated with replicate analyses of the same solution in the former case, and that associated with replicate preparations of solutions from the same original sample (i.e., a coral septum or seawater aliquot) in the latter case. The "pooling" of replicate analyses is commonplace in MC-ICP-MS and was first statistically justified by Albarède et al. (2004), who demonstrated that replicate analyses do indeed adhere to a single distribution. As noted above, we relied on this approach to increase the total number of counts
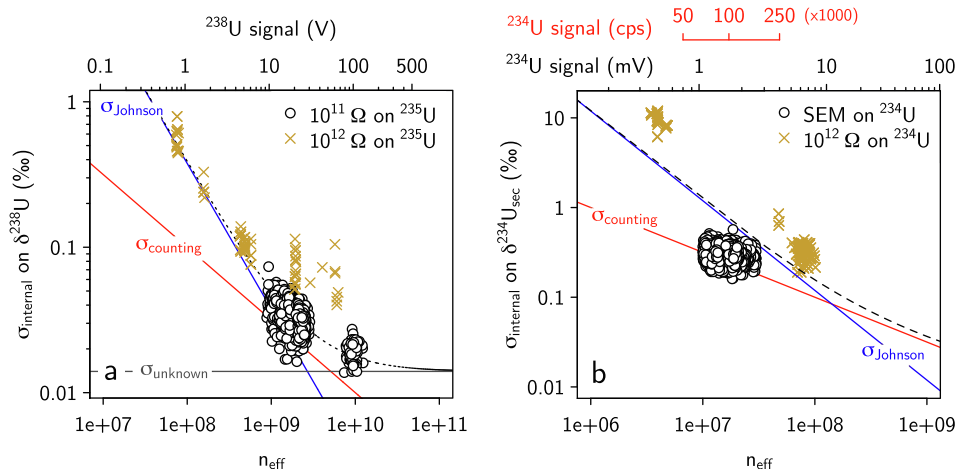
Fig. 3. Limits on internal precision of U isotope analyses. Internal precision on (a) $\delta^{238}U$ and (b) $\delta^{234}U_{sec}$ measurements is limited by Johnson noise ($\sigma_{Johnson}$; blue lines) and counting statistics ($\sigma_{counting}$; red lines). All sample data (white circles) plot at the theoretical maximum internal precision (represented by the dashed black curve, which is the sum of the red and blue lines). Standards analyzed with a 10^{12} Ω amplifier on ^{235}U show poorer internal precision (gold crosses, panel a). The subset of samples for which ^{234}U was measured in a Faraday cup (gold crosses, panel b; 10^{12} Ω amplifier) are limited by both Johnson noise and counting statistics; all other samples for which ^{234}U was measured in the SEM (white circles) were only limited by counting statistics. Theoretical error from Johnson noise was calculated for a 10^{11} Ω amplifier on ^{235}U in panel (a) and 10^{12} Ω amplifier on ^{234}U in panel (b); 10^{11} Ω amplifier was used for ^{238}U in all calculations. Top x-axes denote signal intensity on ^{238}U and ^{234}U in panels (a) and (b), respectively. In panel (b), the secondary (red) top x-axis denotes the signal in cps registered on the SEM for SEM-FAR measurements; the primary (black) top x-axis denotes the signal in mV registered on the Faraday cup for FAR-FAR measurements. For both panels, the signal intensity is directly related to n_{eff} since all analyses were comprised of 50 cycles of 4.194 s each. (For interpretation of the references to colour in this figure legend, the reader is referred to the web version of this article.)

per sample analysis, rather than increase our measurement intensity.

Here we consider two approaches to quantify the contributions to total error that result from the pooling of replicate analyses. First, we follow John and Adkins (2010) in calculating the error-normalized deviates (END's) of replicate analyses. While John and Adkins (2010) calculated END's using measured isotopic ratios, we have modified the calculation to utilize double-spike corrected delta values so that we can observe the ultimate precision of our double-spiked reduced data. We therefore calculate END as

$$END = \frac{\delta U_i - \delta U_j}{\sqrt{\sigma_i^2 + \sigma_j^2}} \qquad (6)$$

where δU_i and δU_j denote the delta values ($\delta^{238}U$, $\delta^{234}U_{sec}$) of individual replicate analyses of a given sample, and σ_i and σ_j are the internal errors associated with these measurements. If the pooled replicate analyses have a variance matching that which is expected given their prescribed errors, then the distribution of all END's calculated for all possible pairs of replicate analyses will have a standard deviation (σ_{END}) of unity. An advantage of casting the intermediate and external error in this way is that relative contributions of error are intuitive to grasp: for our double-spike reduced $\delta^{238}U$ data, we observe σ_{END} of ∼1.6 for replicate analyses of the same solution (Table 1), meaning the internal error would need to be 60 % larger to account for the dispersion of replicate analyses. The σ_{END} of replicate preparations of samples is ∼1.9 (Table 1). These values are slightly lower for $\delta^{234}U_{sec}$ (Table 1).

Second, we calculate a more common metric, the mean squared weighted deviation (MSWD; Wendt and Carl, 1991), as

$$MSWD = \left(\frac{1}{n}\right) \sum_i^n \frac{(\delta U_i - \delta U_{mean})^2}{\sigma_i^2}. \qquad (7)$$

Like σ_{END}, the MSWD has a value of unity when the analytical replicates adhere to the distribution that would be expected given their prescribed errors. If the errors specified are the internal error, then the MSWD is being used in nearly identical fashion to the END. Calculating the MSWD using the same replicates as above gives an average value of 4.05 for $\delta^{238}U$ and 1.66 for $\delta^{234}U_{sec}$ (Table 1), indicating that the actual uncertainty is larger than just the internal error.

One might now ask why the error of pooled replicate analyses is larger than that of single measurements, particularly for $\delta^{238}U$. We note that it is not the case that pooling analyses adds additional error; rather, by making replicate measurements of the same solution, we are able to observe that the dispersion of these measured values is greater than that implied by their internal error. In other words, the internal error does not capture the full uncertainty on the measurement. For this reason, observations of $\sigma_{END} > 1$ highlight the importance of making several replicate analyses of a solution, such that the full error may be captured. To demonstrate that we have indeed accounted for the full error of replicate analyses,

we can again calculate the MSWD, this time using the intermediate or external error. We find that MSWD ∼ 1 for intermediate and external replicates for $\delta^{238}U$ and $\delta^{234}U_{sec}$ (Table 1), meaning that our quoted errors indeed capture the full uncertainty on each measurement.

Finally, we can consider the ways in which our analytical setup differs from prior work, and whether it impacts the limits on our analytical precision. For instance, John and Adkins (2010) reported σ_{END} of 1.04 for replicate Fe isotope analyses, meaning that the total analytical error almost entirely derives from internal error (i.e., Johnson noise and counting statistics). One difference between our analytical approach and theirs is that we employ double spike deconvolution to correct for mass fractionation during sample preparation and analysis. Interestingly, if we repeat the END calculation for our $\delta^{238}U$ data prior to double spike deconvolution (i.e., only using standard-sample bracketing to calculate delta values), we obtain a smaller σ_{END} of ∼1.4 for our intermediate precision. At first glance, this seems to imply that the double spike correction is adding uncertainty. But it is important to note that this increase in σ_{END} (from 1.4 to 1.6 after double spike deconvolution) is accompanied by a decrease in absolute error. Thus, the increase in σ_{END} reflects the fact that, after double spike correction, processes that are not corrected for by standard-sample bracketing and double spike deconvolution (e.g., plasma flicker, instrumental mass bias fluctuations) represent a greater proportion of the residual error.

We further explored whether part of this residual error could be accounted for by utilizing a different mass fractionation law to describe instrumental mass bias. Most double spike work assumes that instrumental mass bias in both TIMS and MC-ICP-MS instruments follows the exponential law, following empirical constraints from multiple elements (Russell et al., 1978; Albarède et al., 2004; Albarède et al., 2015). However, for extremely high-precision analyses, subtle deviations from the exponential law can have resolvable effects (e.g., Hart and Zindler, 1989; Wombacher and Rehkämper, 2003). To test for such effects, we modified our data reduction scheme to utilize the generalized power law (Maréchal et al., 1999). Using different exponents ($-1 < n < 1$) had a negligible effect on the reproducibility of our data (i.e., σ_{END} remained ∼ 1.6), indicating that the combination of standard-sample bracketing and double spiking accounts for most of the mass-dependent fractionation during isotopic analyses, regardless of the assumption on the mass-fractionation law. We therefore conclude that the remaining error derives from non-mass-dependent fluctuations in instrumental mass fractionation.

To track down the source of this remaining error, we can consider a second difference between our work and that of John and Adkins (2010): we used a DSN (Aridus 3), whereas the Fe isotope analyses used a glass cyclonic spray chamber (CSC). While the DSN results in higher sensitivity, the CSC setup has superior signal stability, and it is thus possible that sample introduction with a DSN causes medium-term (i.e., intra-run) changes in mass bias

Table 1
Precision and accuracy of replicate analyses. MSWD = mean squared weighted deviation; σ_{END} = standard deviation of error-normalized deviates (END's). Calculations are presented in **Section 4.2.2**. MSWD was calculated for external replicates with $n_{analyses} \geq 9$. Representative intermediate and external 95 % CI values were calculated from corresponding 2SD value assuming $n_{analyses} = 9$; better precision can be attained if more replicate analyses are performed.

	$\delta^{238}U$				$\delta^{234}U_{sec}$			
	avg. 2SD (‰)	avg. 95 % CI (‰)	MSWD	σ_{END}	avg. 2SD (‰)	avg. 95 % CI (‰)	MSWD	σ_{END}
Internal	N/A	0.068	4.05	N/A	N/A	0.67	1.66	N/A
Intermediate	0.121	0.046	1.04	1.59	0.87	0.33	1.19	1.08
External	0.138	0.052	0.80	1.85	0.95	0.36	0.81	1.38

that affect the reproducibility of replicate analyses. We tested this hypothesis by running a sequence of standards using an identical setup (i.e., same cones, amplifier configuration) but with the glass CSC instead of the DSN, and indeed found σ_{END} of ∼1.0 for intermediate precision on $\delta^{238}U$. We therefore conclude that instabilities in sample introduction with the DSN alone can explain the additional error observed in replicate $\delta^{238}U$ analyses. While running all analyses with a CSC would therefore allow superior precision, U transmission ($U_{measured}/U_{introduced}$) is an order of magnitude lower for the CSC than DSN. This therefore represents a tradeoff that an analyst must assess based on the availability of sample material and the cost of additional standard and spike consumed in bracketing analyses. For the sample-limited nature of the seawater analyses undertaken here, sample introduction via the DSN was determined to be the most reasonable approach. The maximum attained external precision of these analyses (95 % CI of ∼±0.03 ‰ on $\delta^{238}U$) only slightly deviates from that achievable with a CSC (∼±0.02 ‰).

4.3. Analytical accuracy

Having established an approach to precise U isotope analyses, we now must confirm that our data are accurate within the reported precision limits. For $\delta^{238}U$ data, this task is straightforward. Every single sample measurement was bracketed by measurement of a standard solution (CRM-112a) spiked to the same level (3 %), at the same U concentration and same acid molarity as the sample solutions. After correcting sample and standard data individually via the double spike, we then used standard-sample bracketing to determine the $\delta^{238}U$ value. This allows the correction of systematic biases that double spike deconvolution alone cannot handle, such as offsets due to different cones or cup configurations (Tissot and Dauphas, 2015), or non-exponential mass-fractionation (see above).

To confirm that our approach gives accurate results, we compare our $\delta^{238}U$ data from several replicate digests of the BCR-2 geostandard (Table 2) to all previously published values (Weyer et al., 2008; Brennecka and Wadhwa, 2012; Cheng et al., 2013; Murphy et al., 2014; Iizuka et al., 2014; Dahl et al., 2014, 2017, 2019; Tissot and Dauphas, 2015; Holmden et al., 2015; Goldmann et al., 2015; Brennecka et al., 2015, 2018; Andersen et al., 2015; Tissot et al., 2016, 2018, 2019; Lau et al., 2016, 2017; Wang et al., 2018; Avanzinelli et al., 2018; Dang et al., 2016, 2018,2022; Freymuth et al., 2019; Merle et al., 2020). We find that our data ($\delta^{238}U$ = -0.260 ‰ ± 0.016 ‰, $n_{digests}$ = 11 separate digests, $n_{analyses}$ = 142 replicate analyses) closely agree with prior work ($\delta^{238}U$ = -0.262 ‰ ± 0.005 ‰, $n_{digests}$ = 33). Furthermore, all 11 digests that were analyzed individually fall within uncertainty of the literature mean. Collectively, these results demonstrate that our $\delta^{238}U$ analyses are accurate as well as precise.

In the case of $\delta^{234}U_{sec}$ data, achieving analytical accuracy is more complicated. The reason is that the SEM-FAR (cps/V) "yield" calibration is itself a source of uncertainty. Thus, in cases where this calibration is inaccurate but the SEM analysis is very precise due to the large number of counts, the resulting data can easily be inaccurate within the reported analytical precision.

To ensure that we accurately determined the SEM-FAR yield, we performed a manual calibration at the beginning and end of each measurement sequence. We did this by running our same bracketing standard solution in a measurement routine with two subsequences: one where the center cup (^{234}U) signal was diverted to the SEM, and another where the ^{234}U signal was measured in a Faraday cup with a 10^{12} Ω amplifier. In a typical run, we would start and finish with 3 replicates of this "cps/V calibration" method, which would be averaged to determine the yield for that run. We note that while other isotopes could be used to achieve a larger signal on the center cup (e.g., ^{233}U or ^{236}U) and thus a more precise estimate of the cps/V value, measuring the cps/V yield at a higher

intensity would require correction for the non-linearity of the response of the SEM (Richter et al., 2001). As correcting for this non-linearity would require also making measurements at the same intensity as our sample analyses, we circumvented the non-linearity correction by simply determining our cps/V yield at the same intensity as our analyses.

When using this method, we were able to observe the yield diminishing throughout a multi-week analytical session (Fig. 4), as is expected due to degradation of the SEM as a linear function of counts. Since individual yield calibrations are not very precise, owing to the small ^{234}U ion beam (1–2 mV), we ultimately fit a linear trend through the cps/V values as a function of cumulative counts registered by the SEM and used the corresponding values to correct our data through a multi-sequence analytical session (typically 5–15 days long).

We evaluated the accuracy of this method of yield calibration in two ways. First, we measured three samples using a Faraday-Faraday (FAR-FAR) method that did not require a cps/V conversion (as in Andersen et al., 2004, 2010). We did this by running at a higher U concentration (100 ppb for FAR-FAR vs 15 ppb for SEM-FAR measurements) and employing 10^{10} Ω and 10^{12} Ω amplifiers to measure the ^{238}U (∼145 V) and ^{234}U (∼8 mV) signals, respectively. In doing so, we observed that all three samples were measured at identical values within analytical precision via FAR-FAR and SEM-FAR analysis (Fig. 5a). This confirms that our cps/V conversion method indeed gives accurate results.

Second, we generated $\delta^{234}U_{sec}$ data from replicate digests and analyses of BCR-2. We determined a value of $\delta^{234}U_{sec}$ = +0.64 ‰ ± 0.08 ‰ ($n_{digests}$ = 11, $n_{analyses}$ = 142 replicate analyses; Fig. 5b), which includes measurements in four separate analytical sessions (and thus four independent cps/V calibrations) over a span of 19 months. This value is within error of previously reported values (Fig. 5b; Cheng et al., 2013; Tissot and Dauphas, 2015; Tissot et al., 2018, 2019; Avanzinelli et al., 2018) but is more precise because we used much more U per measurement than is typically done in $\delta^{234}U_{sec}$ work (because more U is required for precise $\delta^{238}U$ analysis). We therefore can confidently say that the $^{234}U/^{238}U$ of BCR-2 is not at secular equilibrium, and further suggest that this geostandard can be used as an accuracy test in future $\delta^{234}U_{sec}$ studies.

5. Results

Seawater samples analyzed using the methods described above show subtle heterogeneity in $\delta^{238}U$, and to a lesser extent in $\delta^{234}U_{sec}$ (Table 2). Individual seawater samples from the North Atlantic (GA02 and GA03) display a ∼0.1 ‰ range in measured $\delta^{238}U$ values, from −0.431 ± 0.042 ‰ to −0.337 ± 0.045 ‰. Analyses of samples from the same depths at adjacent stations show good agreement (Fig. 6a). A baseline of about −0.39 ‰ is observed, with the exception of an excursion to more positive values (maximum of about −0.34 ‰) near 1000 m depth (Fig. 6a). This coincides with a drop in absolute U concentration (Fig. 6a), as well as U/salinity. In contrast, $\delta^{234}U_{sec}$ remains constant at all depths and sites, within a range of +144.98 ± 0.23 ‰ to +146.22 ± 0.43 ‰ (Fig. 6a). Four D. dianthus specimens show very close agreement with the $\delta^{238}U$ values of ambient seawater (Fig. 6a); however, two specimens deviate in $\delta^{234}U_{sec}$.

Seawater samples from the South Pacific (GP13) show a narrower $\delta^{238}U$ range of ∼0.05 ‰ (−0.387 ± 0.029 ‰ to −0.338 ± 0.030 ‰). A narrow $\delta^{234}U_{sec}$ range is also observed, from +145.14 ± 0.04 ‰ to +145.76 ± 0.32 ‰ (Fig. 6b). A single D. dianthus specimen at this site shows excellent agreement with both $\delta^{238}U$ and $\delta^{234}U_{sec}$ (Fig. 6b). Several replicate analyses of different septa on a D. dianthus specimen from the TN-228 cruise also show good agreement in $\delta^{238}U$ and $\delta^{234}U_{sec}$ when compared to the GP13 seawater data (Fig. 7).

Table 2
Uranium data generated in this study. All U concentration data have 95 % CI < 0.01 ng/g; however, we note that a larger systematic uncertainty likely exists due uncertainties in the dilution of the CRM-112a and IRMM-3636 spike solutions. This uncertainty would not affect the trends observed here, but could slightly offset the absolute U content of the samples in a systematic fashion.

North Atlantic

GEOTRACES

cruise	latitude	longitude	depth (m)	$\delta^{238}U$	95 % CI	$\delta^{234}U_{sec}$	95 % CI	salinity	U (ng/g)	n
GA03	35.4178	293.4735	235.7	−0.387	0.036	145.73	0.35	36.595	3.02	8
GA03	39.6859	290.1870	420	−0.400	0.054	145.56	0.33	35.098	3.04	9
GA03	35.4178	293.4735	422.5	−0.414	0.036	145.75	0.35	36.511	3.04	8
GA03	39.6859	290.1870	475	−0.358	0.045	146.22	0.43	35.068	3.05	5
GA03	39.6859	290.1870	526	−0.380	0.044	144.98	0.23	35.054	2.98	13
GA03	35.4178	293.4735	552.3	−0.355	0.046	145.27	0.27	36.207	3.14	13
GA03	39.6859	290.1971	600	−0.392	0.038	145.65	0.32	35.023	2.99	8
GA03	39.6859	290.1971	665	−0.373	0.038	145.63	0.32	34.994	2.93	8
GA03	35.4178	293.4735	803.6	−0.358	0.046	145.33	0.27	35.344	2.99	13
GA03	39.6859	290.1971	825	−0.355	0.040	146.15	0.28	34.962	2.89	11
GA02	49.7218	317.5523	1012	−0.337	0.045	145.71	0.25	34.935	2.83	7
GA02	51.8203	314.2675	1014	−0.347	0.046	145.57	0.27	34.893	2.93	13
GA02	51.8203	314.2675	1258	−0.405	0.047	145.57	0.28	34.896	3.05	12
GA02	49.7218	317.5523	1262	−0.357	0.048	145.65	0.27	34.914	3.05	6
GA03	39.6859	290.1971	1501	−0.361	0.048	145.74	0.30	34.955	2.91	11
GA02	49.7218	317.5523	1517	−0.407	0.040	145.91	0.26	34.920	2.91	7
GA02	51.8203	314.2675	1521	−0.431	0.042	145.40	0.21	34.912	3.04	14
GA02	54.0634	314.1649	1521	−0.400	0.051	145.95	0.31	34.906	3.04	10
GA03	39.6859	290.1971	1671	−0.386	0.037	145.58	0.23	34.953	3.01	7
GA02	54.0634	314.1649	1758	−0.390	0.052	145.76	0.31	34.909	3.06	10
GA02	49.7218	317.5523	1771	−0.392	0.040	145.90	0.26	34.923	3.02	7
GA02	51.8203	314.2675	1773	−0.407	0.047	145.22	0.17	34.912	2.91	14
GA03	39.6859	290.1971	1800	−0.402	0.071	145.74	0.52	34.955	3.00	8
GA03	39.6859	290.1971	2000	−0.382	0.067	145.06	0.52	34.948	3.00	8
GA02	51.8203	314.2675	2003	−0.413	0.047	145.49	0.17	34.910	2.89	14
GA02	49.7218	317.5523	2024	−0.386	0.035	146.12	0.23	34.919	3.01	9
GA03	39.6859	290.1971	2050	−0.413	0.083	145.49	0.38	34.947	2.97	3

D. dianthus

sample	latitude	longitude	depth (m)	$\delta^{238}U$	95 % CI	$\delta^{234}U_{sec}$	95 % CI	U (ng/g)	n
7923	39.725	290.617	1953–2220	−0.395	0.042	141.33	0.29	3.51	9
78461	38.488	286.973	1990–2175	−0.366	0.041	145.19	0.21	3.91	21
62306	39.775	290.262	1675	−0.386	0.064	141.56	0.26	4.22	6
62309	40.379	292.344	430–613	−0.404	0.030	145.78	0.31	3.39	15

South Atlantic

GEOTRACES

cruise	latitude	longitude	depth (m)	$\delta^{238}U$	95 % CI	$\delta^{234}U_{sec}$	95 % CI	salinity	U (ng/g)	n
GA02	−48.968	311.121	301	−0.407	0.043	145.37	0.30	34.053	3.03	9
GA02	−48.968	311.121	404	−0.374	0.024	145.08	0.37	34.114	2.87	9
GA02	−48.968	311.121	502	−0.356	0.044	144.90	0.39	34.207	2.97	9
GA02	−48.968	311.121	750	−0.396	0.046	145.66	0.16	34.372	3.64	10
GA02	−48.968	311.121	1014	−0.358	0.045	145.52	0.40	34.513	2.99	8
GA03	−48.968	311.121	1267	−0.379	0.042	145.54	0.26	34.625	3.00	7

D. dianthus

sample	latitude	longitude	depth (m)	$\delta^{238}U$	95 % CI	$\delta^{234}U_{sec}$	95 % CI	U (ng/g)	n
47409	−54.483	320.633	659–686	−0.366	0.034	145.10	0.23	4.71	21

South Pacific

GEOTRACES

Cruise	latitude	longitude	depth (m)	$\delta^{238}U$	95 % CI	$\delta^{234}U_{sec}$	95 % CI	salinity	U (ng/g)	n
GP13	−29.999	173.000	15	−0.376	0.036	145.37	0.30	35.642	2.92	21
GP13	−29.999	173.000	30	−0.361	0.038	145.29	0.23	35.641	3.01	25
GP13	−29.999	173.000	50	−0.387	0.029	145.27	0.21	35.640	3.01	21
GP13	−29.999	173.000	75	−0.354	0.027	145.43	0.23	35.641	3.05	25
GP13	−29.999	173.000	100	−0.357	0.030	145.48	0.25	35.638	3.03	21
GP13	−29.999	173.000	150	−0.360	0.028	145.43	0.35	35.601	3.07	21
GP13	−29.999	173.000	200	−0.369	0.026	145.15	0.40	35.559	2.99	23
GP13	−29.999	173.000	300	−0.338	0.030	145.21	0.20	35.434	3.08	21
GP13	−29.999	173.000	500	−0.372	0.027	145.51	0.31	34.996	2.97	20
GP13	−29.999	173.000	750	−0.374	0.033	145.63	0.30	34.644	2.94	19
GP13	−29.999	173.000	1000	−0.375	0.024	145.34	0.31	34.434	2.90	20
GP13	−29.999	173.000	1450	−0.379	0.026	145.76	0.32	34.554	2.86	19

D. dianthus

sample	latitude	longitude	depth (m)	$\delta^{238}U$	95 % CI	$\delta^{234}U_{sec}$	95 % CI	U (ng/g)	n
94071	−30.717	173.280	590–640	−0.370	0.031	145.44	0.34	3.71	9
TN228	−44.8	150.3	2395	−0.331	0.044	145.31	0.42	5.75	13
TN228	−44.8	150.3	2395	−0.361	0.073	145.21	0.41	5.67	11
TN228	−44.8	150.3	2395	−0.385	0.053	145.20	0.28	5.28	12

sample				$\delta^{238}U$	95 % CI	$\delta^{234}U_{sec}$	95 % CI	U (ng/g)	n
TN228	−44.8	150.3	2395	−0.380	0.074	145.11	0.34	5.34	9
TN228	−44.8	150.3	2395	−0.402	0.069	145.06	0.35	5.33	9
TN228	−44.8	150.3	2395	−0.324	0.034	145.20	0.40	5.23	8
TN228	−44.8	150.3	2395	−0.338	0.067	145.10	0.36	5.34	9
TN228	−44.8	150.3	2395	−0.366	0.050	145.34	0.31	5.08	12
TN228	−44.8	150.3	2395	−0.425	0.058	144.03	0.34	5.12	9
TN228	−44.8	150.3	2395	−0.361	0.061	145.26	0.23	4.92	9
TN228	−44.8	150.3	2395	−0.355	0.083	144.70	0.30	4.67	8
TN228	−44.8	150.3	2395	−0.373	0.045	145.37	0.35	4.68	8
TN228	−44.8	150.3	2395	−0.374	0.051	144.75	0.38	4.66	9
TN228	−44.8	150.3	2395	−0.344	0.045	144.89	0.40	4.69	8
TN228	−44.8	150.3	2395	−0.377	0.041	144.58	0.40	4.73	9
TN228	−44.8	150.3	2395	−0.365	0.051	145.70	0.35	4.47	8
TN228	−44.8	150.3	2395	−0.400	0.060	145.41	0.26	4.56	9
TN228	−44.8	150.3	2395	−0.371	0.038	145.50	0.20	4.64	8
TN228	−44.8	150.3	2395	−0.375	0.075	145.25	0.22	4.58	10
TN228	−44.8	150.3	2395	−0.373	0.079	144.94	0.33	4.63	9

BCR-2

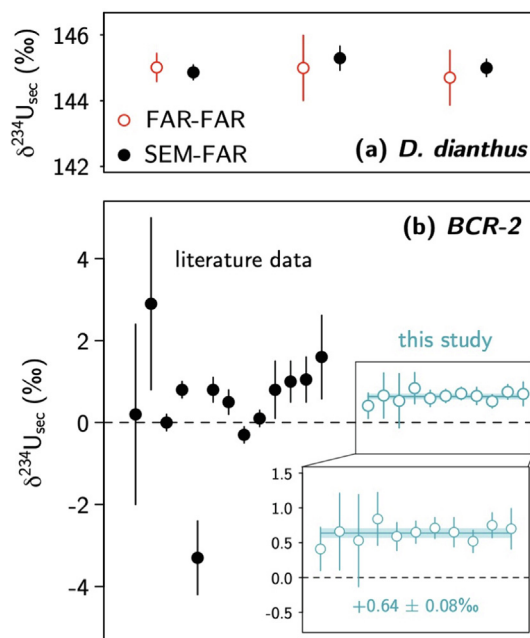| sample	$\delta^{238}U$	95 % CI	$\delta^{234}U_{sec}$	95 % CI	U (ng/g)	n
BCR-2	−0.291	0.047	0.41	0.31	1.63	9
BCR-2	−0.226	0.036	0.66	0.55	1.61	4
BCR-2	−0.229	0.032	0.53	0.67	1.71	4
BCR-2	−0.235	0.060	0.84	0.38	1.74	8
BCR-2	−0.277	0.034	0.71	0.15	1.59	19
BCR-2	−0.264	0.025	0.65	0.21	1.59	16
BCR-2	−0.243	0.025	0.52	0.16	1.59	21
BCR-2	−0.299	0.040	0.59	0.20	1.59	14
BCR-2	−0.269	0.022	0.65	0.16	1.59	25
BCR-2	−0.265	0.036	0.75	0.18	1.58	11
BCR-2	−0.263	0.036	0.70	0.29	1.58	11
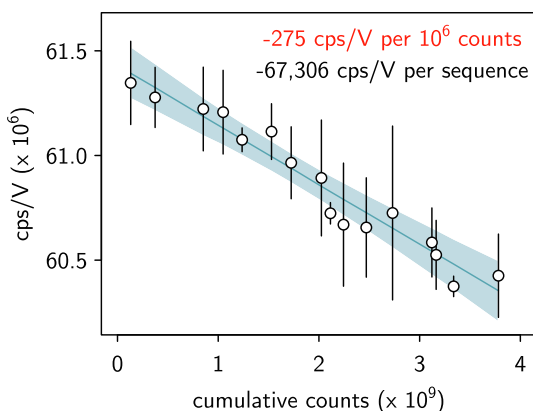
Fig. 4. SEM-Faraday cup yield calibration through 16 consecutive analytical sequences. One sequence was run per day and the yield was measured at the beginning and end of each sequence; the points and error bars represent the mean and 95 % CI of these yield determinations. The total number of counts registered in the SEM per session were then tallied and the yield determinations were fit against cumulative counts. Solid line denotes linear trend through data with 95 % CI in shaded region as determined by Monte Carlo simulation. We find that the yield diminishes by about 275 cps/V per million counts.

Fig. 5. Accuracy of $\delta^{234}U_{sec}$ analyses. SEM = secondary electron multiplier used to measure ^{234}U; FAR = Faraday cup used to measure ^{234}U. Panels denote: (a) comparison of SEM-FAR and FAR-FAR measurements of three *D. dianthus* specimens from Cruise TN-228, and (b) comparison of measured $\delta^{234}U_{sec}$ values for USGS BCR-2 geostandard with literature reports (references in **Section 4.3**).

Seawater samples from the South Atlantic (GA02) show a similarly narrow range of $\delta^{238}U$ (−0.407 ± 0.043 ‰ to −0.356 ± 0.044 ‰) and $\delta^{234}U_{sec}$ values (+144.90 ± 0.39 ‰ to +145.54 ± 0.16 ‰). One nearby coral shows $\delta^{238}U$ (−0.366 ± 0.034 ‰) and $\delta^{234}U_{sec}$ (+144.91 ± 0.33 ‰) values that agree within analytical precision.

6. Discussion

6.1. Homogenous $\delta^{234}U_{sec}$, heterogeneous $\delta^{238}U$: What is the mechanism?

Our high-precision survey of seawater U isotope ratios has surprisingly revealed resolvable differences in $\delta^{238}U$ values, and to a lesser extent in $\delta^{234}U_{sec}$ values, along depth profiles. Here, we consider what mechanism(s) might be driving this isotopic variability. These can be divided into two categories: (i) mixing of heterogeneous water masses (i.e., conservative behavior), and (ii) *in-situ* chemical processing (i.e., non-conservative behavior).

To assess the first possibility, we can use the narrow range of $\delta^{234}U_{sec}$ values as a clue. It is known that rivers deliver U to the ocean with highly variable $\delta^{234}U_{sec}$ (range of > 1000 ‰; Andersson et al., 1995; Chabaux et al., 2001, 2003; Robinson
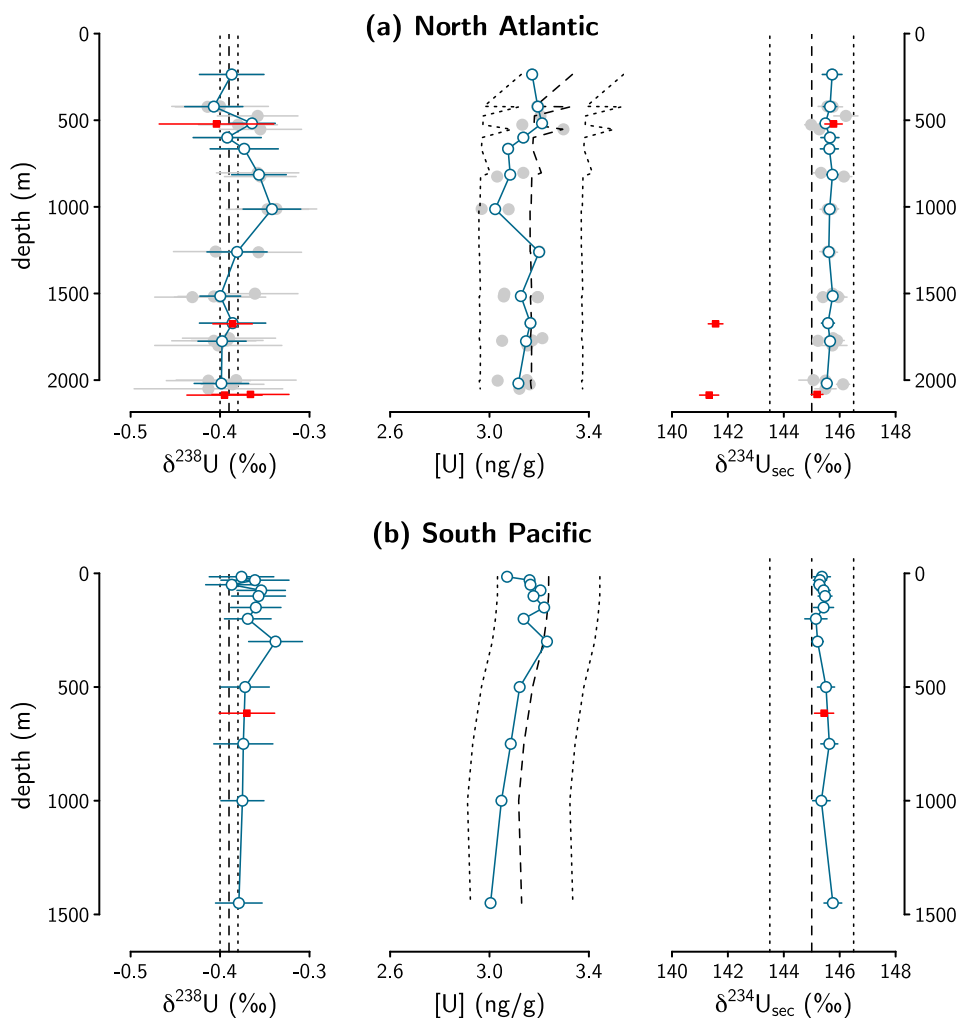
Fig. 6. Depth profiles in the (a) North Atlantic and (b) South Pacific. Circles denote seawater samples; squares denote coral samples. Grey circles represent individual preparations of seawater that were averaged for a given depth. Dashed and dotted lines denote the following means and associated uncertainty: in δ^{238}U plots, published global seawater value (-0.39 ± 0.01 ‰; Tissot and Dauphas, 2015); in [U] plots, predicted [U] assuming U/salinity as in Owens et al (2011) ([U] = (0.100 ± 0.006) * S – (0.326 ± 0.206); in δ^{234}U$_{sec}$ plots, global re-normalized coral and seawater value ($+145.0 \pm 1.5$ ‰; Chutcharavan et al., 2018). South Atlantic data not plotted due to low sample density. Associated sample metadata are presented in Table 2.

et al., 2004b; Andersen et al., 2007, 2016); by comparison, the range of riverine δ^{238}U values is much smaller (<1‰; Andersen et al., 2016). It follows that the mixing of riverine signatures into the global seawater reservoir should yield steeper gradients for δ^{234}U$_{sec}$ than δ^{238}U. Indeed, Andersen et al (2007) observed the δ^{234}U$_{sec}$ signature of riverine input in the Arctic ocean. In that study, a δ^{234}U$_{sec}$ range of > 10 ‰ was observed, which corresponded to an up to > 10 % contribution of river water in the studied samples (i.e., a salinity range from 35 to 30 psu). In contrast, the samples studied here are little affected by riverine inputs, evidenced in part by a much narrower range of salinity (34.5 to 36.0 psu) that is more closely influenced by water mass evaporation-precipitation balance than freshwater input. Consistently, very little variability in δ^{234}U$_{sec}$ is seen in the samples – both within depth profiles at each site, and across ocean basins (Fig. 6). Put another way, the narrow distribution of δ^{234}U$_{sec}$ values implies a negligible effect from mixing of isotopically variable riverine inputs on seawater δ^{238}U values.

A second possible U source – which is considerably smaller in global magnitude (Dunk et al., 2002) – is aeolian dust deposition. If aeolian U were deposited (and solubilized) near any of our sample sites, it could act as a source of crustal U (δ^{238}U = −0.29 ‰; δ^{234}U$_{sec}$ = 0 ‰; Tissot and Dauphas, 2015) to seawater. The Atlantic

Ocean receives considerable dust input from the Sahara Desert, though our Atlantic sites are farther north than the region of maximum Saharan dust deposition (e.g., Menzel Barraqueta et al., 2019). Our Pacific site is also close to a region of significant dust deposition from the Australian continent (Ellwood et al., 2018; Nguyen et al., 2019). Mixing of a detrital end-member into seawater at either location would add U that is slightly isotopically heavier in δ^{238}U, and at secular equilibrium for δ^{234}U$_{sec}$, giving a shallow positive slope in δ^{238}U vs [U] space and a steep negative slope in δ^{234}U$_{sec}$ vs [U] space. As noted above, the narrow range of δ^{234}U$_{sec}$ values observed at our sites argues against any significant continental U input, as contributions of even a few percent of continental U would create δ^{234}U$_{sec}$ deviations of several permil. Thus, the observed variability in the ratio of the long-lived isotopes of U (δ^{238}U) in our samples more likely derives from other processes.

We thus turn our attention to the possibility that chemical reactions occurring within the ocean are driving the observed δ^{238}U variability. There are multiple reactions that may fractionate U isotopes in the ocean (Andersen et al., 2017), including reductive immobilization, adsorption to particulates, and incorporation into authigenic minerals; discerning which is (are) the most likely driver(s) of the observed signatures first requires achieving the right sign of isotopic effect and U mass balance. A natural starting
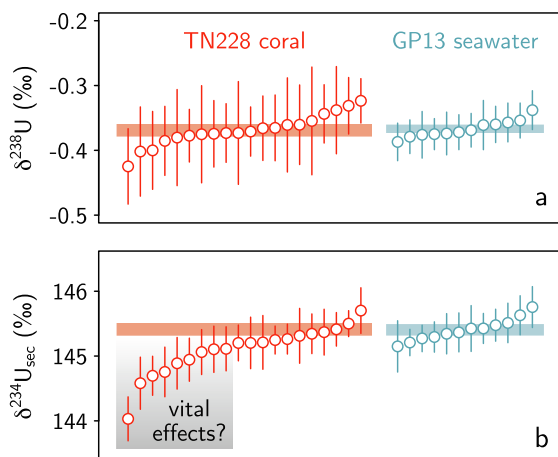
Fig. 7. Comparison of TN-228 coral and GP13 seawater data. Shading denotes mean and 95% confidence interval for coral and seawater samples. Grey shading in panel (b) denotes samples whose $\delta^{234}U_{sec}$ may have been affected by internal ^{234}U partitioning, which were excluded from the calculation of the mean coral $\delta^{234}U_{sec}$ value.

place is to consider the reaction that is thought (e.g., Lau et al., 2019) to exert the largest isotopic leverage on the marine $\delta^{238}U$ mass balance: U reduction in anoxic/euxinic environments. In sediments overlain by anoxic bottom waters, U is reductively immobilized with an isotopic effect of $\sim+0.6$ ‰ (Holmden et al., 2015; Rolison et al., 2017; Lau et al., 2020). This sink accounts for ~20 % of U burial (Morford and Emerson, 1999; Dunk et al., 2002) and depletes the ocean of ^{238}U, driving seawater $\delta^{238}U$ to a value lower than that of riverine inputs (-0.30 ± 0.04 ‰; Andersen et al., 2016). Thus, the isotopic signature of U reduction would be a positive correlation between $\delta^{238}U$ and [U] or [U]/salinity. Strikingly, in both the North Atlantic and South Pacific datasets (South Atlantic not considered here due to sparse data), such a positive correlation is observed (Fig. 8). An illustrative calculation can be made assuming that U is removed from seawater via U reduction with a +0.6 ‰ fractionation. The slope of such a U removal process (red dashed lines, Fig. 8) closely matches the observed trends.

Is local U reduction influencing seawater $\delta^{238}U$ values at these sites? Both the North Atlantic and South Pacific stations (Fig. 2) are far from settings that are thought to make the dominant contributions to anoxic U burial, which include restricted basins such as the Black Sea (Rolison et al., 2017), Saanich Inlet (Holmden et al., 2015) and Cariaco Basin (Andersen et al., 2014). Furthermore, U reduction is thought to predominantly occur at the sediment–water interface (see, e.g., Lau et al., 2020), which is reflected by the $\sim2\times$ smaller (Clark and Johnson, 2008) expressed isotopic fractionation (+0.6 ‰) than is expected due to nuclear field shift effects (+1.3 ‰; Bigeleisen, 1996). Collectively, these observations make it seem unlikely that local U reduction could explain the observed $\delta^{238}U$ trend. Instead, it would seem more likely that the observed $\delta^{238}U$ variability reflects mixing of water masses that are more and less impacted by the process of anoxic U reduction. Such mixing must occur on kyr timescales to propagate the isotopic effect of U reduction in anoxic environments into the global ocean. Thus, we infer that we are most likely observing such an effect in the $\delta^{238}U$ vs [U] correlations (Fig. 8) at the sites studied here, although we cannot explicitly constrain the proximity of the site(s) of U reduction.

In addition to the regional/global impact of anoxic U reduction, there may also be local effects superimposed. For instance, at ~1000 m in the North Atlantic data, $\delta^{238}U$ values go heavier while [U] and [U]/salinity decrease. This implies a process that removes isotopically light U from solution – the opposite direction of U

reduction. One possibility is U adsorption to organic matter, which is associated with a fractionation of -0.2 ‰ to -0.8 ‰ (Holmden et al., 2015; Chen et al., 2020). However, organic matter export flux peaks in the photic zone, much shallower than ~1000 m where the U removal and isotopic fractionation is observed. Furthermore, regeneration of U either adsorbed to organic matter or co-precipitated with carbonate – i.e., remineralization in either the organic or inorganic component of the biological pump – would also not provide a sufficient explanation, as these processes would add U to deeper waters. A more likely process is U adsorption onto Fe- and/or Mn-oxides, in which lighter isotopes are known to adsorb with a fractionation of ~-0.24 ‰ for $\delta^{238}U$ (Brennecka et al., 2011; Goto et al., 2014; Wang et al., 2016), and which is thought to remove up to ~10 % of U from the ocean (Morford and Emerson, 1999; Dunk et al., 2002). Using the observed U depletion at ~1000 m, an illustrative calculation can be made to determine whether U removal via adsorption on Fe- and/or Mn-oxides is a plausible mechanism for the observed isotopic trend. Removal of ~10 % of local U via such a process would result in an effect of ~0.03 ‰, which roughly matches the magnitude of the observed $\delta^{238}U$ excursion (~0.04 ‰; Fig. 8**ab**).

This inference of U adsorption onto Fe- or Mn- oxides is further supported by the published particulate data from the GA02 cruise. At Station 6 (58.602°N, -39.705°E), a sharp Fe(OH)$_2$ maximum is observed at 1000 m depth that is not observed at 500 or 1500 m depth (Stichel et al., 2020). While particulate data do not exist for the GA02 stations studied here (8, 9 and 10), we can speculate that similar particulate distributions exist at these nearby sites and are driving the observed U depletion and isotopic fractionation. Further detailed work to track U isotopes across regions of high particulate content will help to clarify the role of this process in generating water mass $\delta^{238}U$ heterogeneity. In any case, it is clear that these samples experienced a local chemical processing that over-printed the global positive correlation between $\delta^{238}U$ and [U].

We note that the isotopically fractionating processes above do indeed affect $^{234}U/^{238}U$ as well (Bigeleisen, 1996). However, (i) we lack the analytical precision to resolve such an effect (<0.1 ‰), and (ii) such small effects are typically over-printed by the large variability due to mixing of U reservoirs of different age and weathering provenance, and thus different $^{234}U/^{238}U$ ratios. Instead of positive correlations, we in fact observe weak negative correlations between $\delta^{234}U_{sec}$ and [U] (Fig. 9). The mechanisms driving this $^{234}U/^{238}U$ variability could include (i) mixing of ^{234}U-enriched riverine inputs with a seawater end-member, (ii) subtle isotopic fractionation via the pathways noted above (U reduction and adsorption to Fe- or Mn-oxides), (iii) diffusion of ^{234}U-rich porewaters into the ocean (Ku, 1965; Henderson, 2002), and (iv) decay of ^{234}U in seawater creating subtle heterogeneity as it is mixed throughout the ocean. It is possible that small contributions from each of these mechanisms gives rise to the observed trend, but disentangling their relative contributions is not possible given the massive variability in the $\delta^{234}U_{sec}$ of riverine inputs.

Given this subtle variability in seawater $\delta^{238}U$ and $\delta^{234}U_{sec}$ values, we can re-assess the meaning of "global" seawater U isotopic compositions. As for U concentration (Chen et al., 1986; Owens et al., 2011) and other conservative elemental and isotopic tracers (e.g., Re; Anbar et al., 1992; Dickson et al., 2020), it is perhaps most appropriate to report the $\delta^{238}U$ and $\delta^{234}U_{sec}$ value normalized to a salinity of 35, which conventionally represents the average salinity of seawater. While certain water masses may deviate in their U isotopic composition, this global mean value is of use when considering the isotopic mass balance of the ocean at large. If we only consider samples with $34.9 < S < 35.1$ and that fall within 1σ of the mean U/salinity of our dataset (Fig. 10), we obtain 35-psu-normalized $\delta^{238}U$ values of -0.395 ± 0.011 ‰ in the North Atlantic and -0.372 ± 0.027 ‰ in the South Pacific. These numbers are
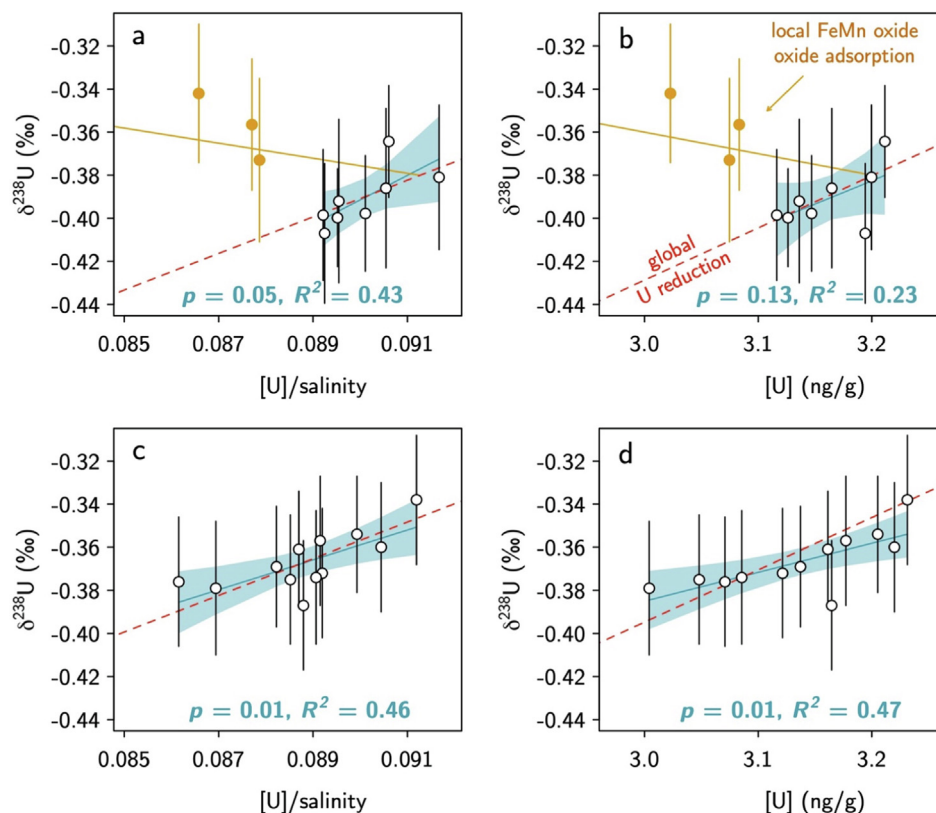
Fig. 8. $\delta^{238}U$ vs [U]/salinity and [U] in (a,b) North Atlantic and (c,d) South Pacific. In both basins, $\delta^{238}U$ positively correlates with [U]/salinity and [U] concentration. These positive correlations are depicted as linear regression lines with 95 % confidence intervals shaded (p and R^2 values reported in each panel). The positive correlation is best explained by the global isotopic impact of U reduction in anoxic sediments with a fractionation of +0.6 ‰ (Andersen et al., 2017; Lau et al., 2019); red dashed lines denote isotopic trend of this removal pathway. In the North Atlantic, anomalous samples that likely show effects of U adsorption to Fe- or Mn- oxides are shown in orange. Solid orange lines in (a) and (b) denote isotopic trend of U removal onto Fe- or Mn- oxides with an isotopic effect of −0.24 ‰ (Goto et al., 2014). (For interpretation of the references to colour in this figure legend, the reader is referred to the web version of this article.)

slightly divergent, albeit in agreement with the prior estimate of the global mean seawater $\delta^{238}U$ value (−0.392 ± 0.005 ‰; Tissot and Dauphas, 2015). The fact that the Atlantic and Pacific samples show the same $\delta^{238}U$ vs [U] slope, but have different y-intercepts, suggests that the two basins have different "initial" $\delta^{238}U$ compositions (due to variable riverine input to each basin and/or different extent of U reduction occurring in each basin). We thus recommend the volume-weighted (~70 % Pacific, ~30 % Atlantic) average of these values (−0.379 ± 0.023 ‰) as the global mean salinity-normalized seawater $\delta^{238}U$ value based on the data generated in this study.

Undertaking the same calculation for $\delta^{234}U_{sec}$, we obtain 35-psu-normalized values of +145.65 ± 0.20 ‰ in the North Atlantic and +145.51 ± 0.31 ‰ in the South Pacific. These values are in close agreement with each other, and within error of (albeit more precise than) a recently compiled average coral and seawater $\delta^{234}U_{sec}$ value (+145.0 ± 1.5 ‰; Chutcharavan et al., 2018 - which includes re-normalized data from Edwards et al., 1987a; Stirling et al., 1995; Robinson et al., 2004a; Andersen et al., 2010 and others). We thus recommend the volume-weighted average of these values (+145.55 ± 0.28 ‰) as the global mean seawater $\delta^{234}U_{sec}$ value.

6.2. Deep-sea corals as an archive of seawater U isotope ratios

Having now thoroughly examined the U isotopic composition of seawater at a local and global scale, we can ask whether modern deep-sea corals record the composition of ambient seawater to within our analytical precision. While prior work has found that scleractinian corals record seawater $\delta^{238}U$ (Chen et al., 2018b;

Tissot et al., 2018) and $\delta^{234}U_{sec}$ values (Chen et al., 1986; Robinson et al., 2006), it has remained unclear whether (i) these calibrations would hold up to the high-precision analyses undertaken here, and (ii) these archives might record subtle U isotope heterogeneity in modern seawater.

As noted above (**Section 5**), we found that modern *D. dianthus* specimens closely record seawater $\delta^{238}U$ and $\delta^{234}U_{sec}$ at all sites (Fig. 6), with a few important exceptions that will be discussed below. To consider these data in aggregate, we averaged the coral compositions at each site and plotted them alongside histograms of seawater data (Fig. 11). We observe that (i) averaged coral compositions provide a robust record of the average seawater U isotopic composition per site, and (ii) basinal averages show subtle trends in both the coral and seawater data that match the directionality (negative $\delta^{238}U$ vs $\delta^{234}U_{sec}$ correlation) observed within sites (Figs. 8, 9). We can also consider the expanded dataset available in the South Pacific, where several replicate analyses (including different septa and intra-septum sub-sampling) were conducted on a coral from the Tasmanian seamounts. These data reveal a striking match in $\delta^{238}U$ values, and to a lesser extent $\delta^{234}U_{sec}$ values, between coral and seawater (Fig. 7). For comparison, we note the agreement between coral and seawater $\delta^{238}U$ values observed here (to within an analytical precision of ~0.03 ‰) is an order of magnitude smaller than the observed range of agreement between seawater and sedimentary carbonates (0 to +0.6 ‰; Chen et al., 2018a; Tissot et al., 2018).

While this close agreement between corals and seawater is quite promising for precise paleoenvironmental reconstructions using these biological archives, it is important to carefully evaluate
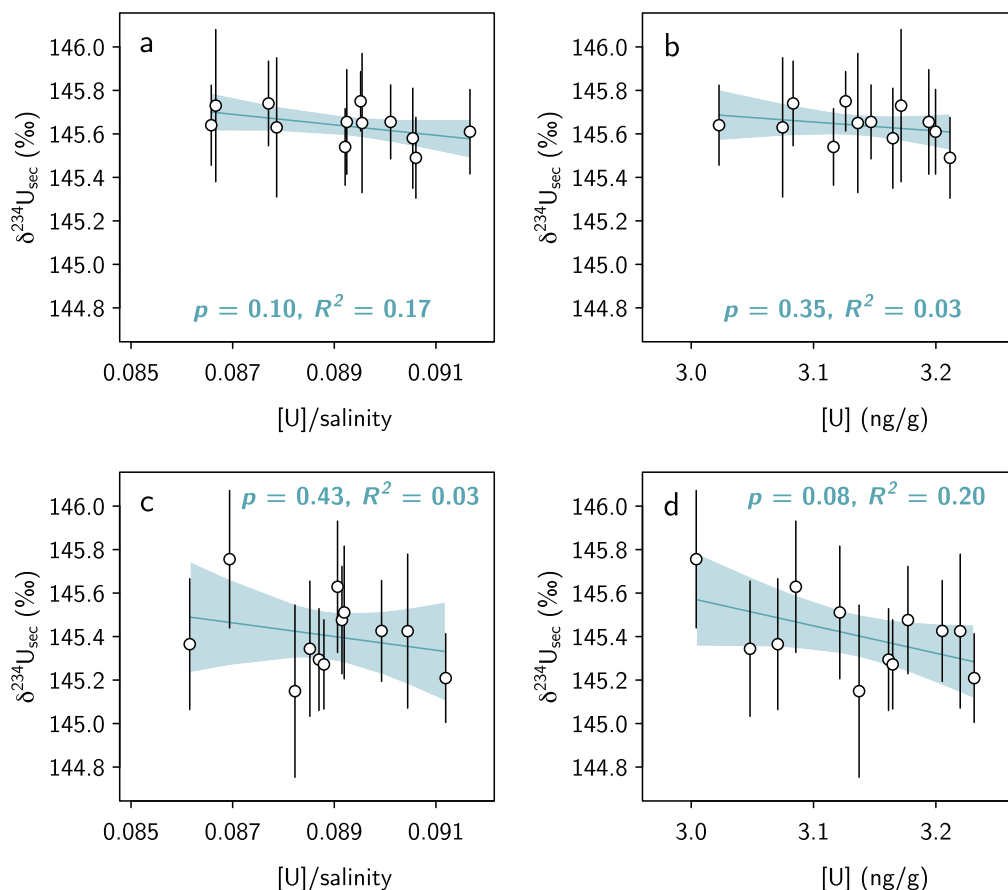
Fig. 9. $\delta^{234}U_{sec}$ **vs [U]/salinity and [U] in (a,b) North Atlantic and (c,d) South Pacific.** In both basins, $\delta^{234}U_{sec}$ negatively correlates with [U]/salinity and [U] concentration, albeit weakly. These negative correlations are depicted as linear regression lines with 95% confidence intervals shaded (*p* and R^2 values reported in each panel). These linear correlations may reflect mixing of subtle marine isotopic heterogeneity and a lack of *in situ* water column chemistry effects observed on $\delta^{234}U_{sec}$.
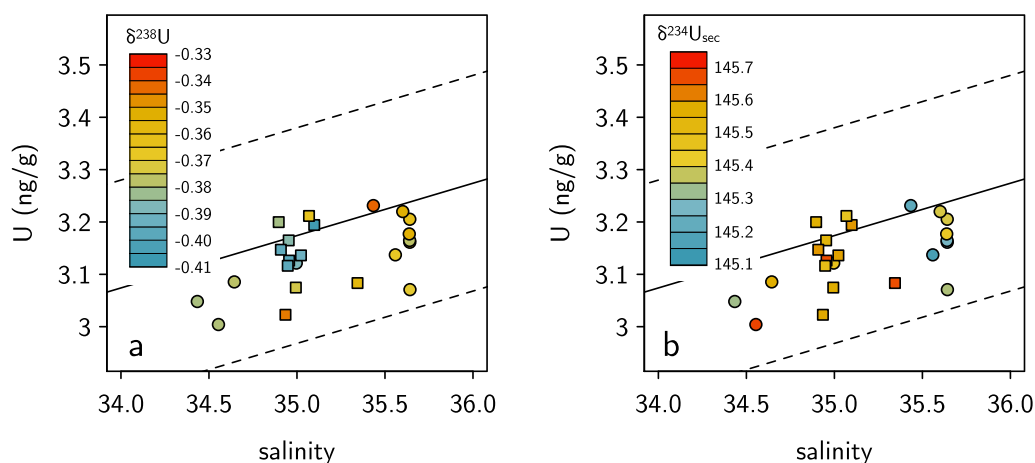

Fig. 10. Uranium concentration versus salinity. Solid and dashed lines denote predicted [U] assuming U/salinity as in Owens et al (2011) ([U] = (0.100 ± 0.006) * S − (0.326 ± 0.206). Coloration of data points reflects corresponding (a) $\delta^{238}U$ and (b) $\delta^{234}U_{sec}$ values. Squares denote North Atlantic data; circles denote South Pacific data.

the limitations of deep-sea corals as an archive of both $\delta^{238}U$ and $\delta^{234}U_{sec}$. We first consider the deviant $\delta^{234}U_{sec}$ data observed in some North Atlantic corals (Fig. 6**b**) and in the TN228 data (Fig. 7**b**). While most coral analyses closely match the $\delta^{234}U_{sec}$ of ambient seawater, some deviate toward more negative values. There are three possible explanations for these values: (i) the coral U pool has been slightly contaminated by detrital U, which would have a large impact on $\delta^{234}U_{sec}$ (assuming detrital U is at secular

equilibrium), but not $\delta^{238}U$; (ii) the bulk coral does not capture the seawater $\delta^{234}U_{sec}$ value due to "vital effects", and (iii) the sub-sampled portion of the coral does not match the composition of the bulk coral, but the latter faithfully records the seawater $\delta^{234}U_{sec}$ value.

The first possibility is unlikely, since the dissolution method (weak acetic acid followed by centrifugation) should not have allowed detrital U to enter the U pool analyzed for the coral
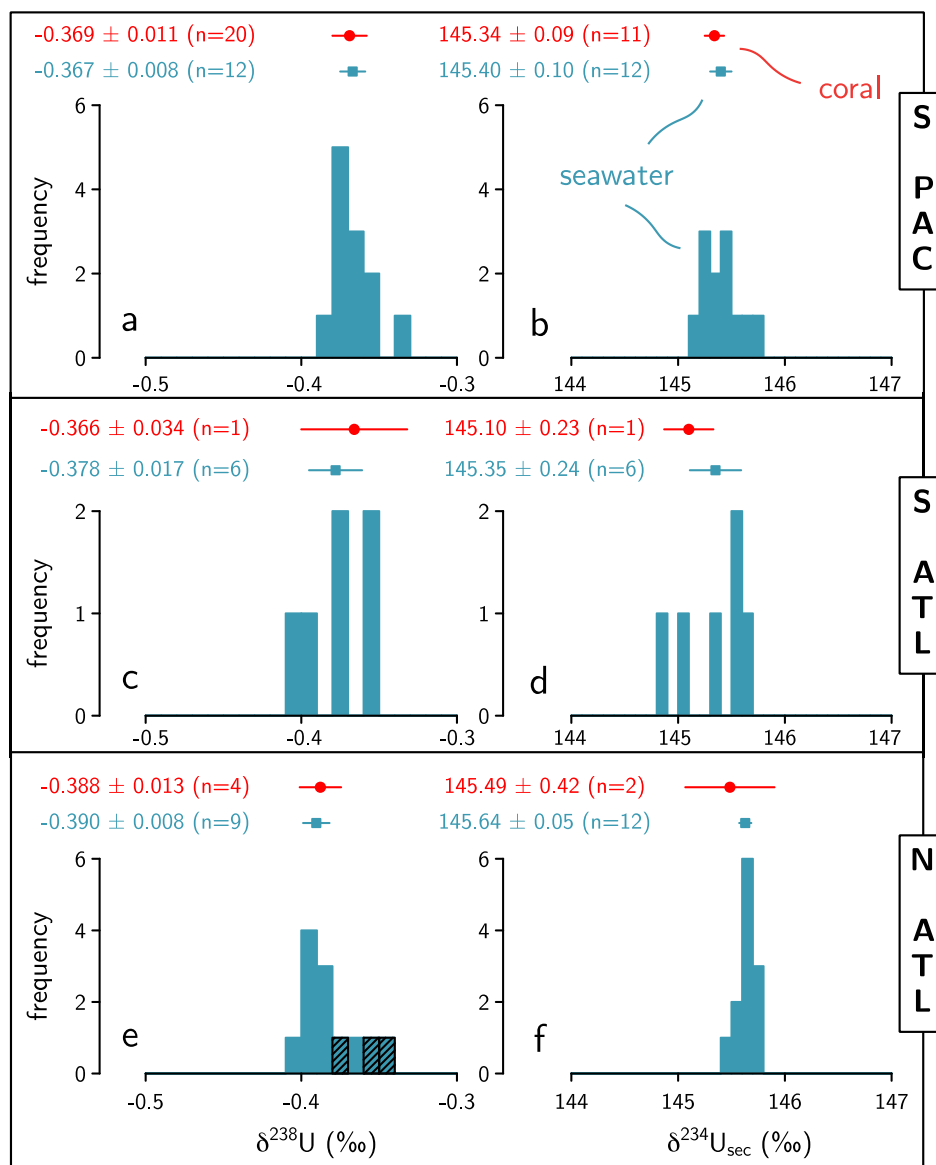
Fig. 11. Comparison of seawater and coral U isotope data across ocean basins. Histograms denote seawater measurements; blue squares represent mean seawater values per site with 2SE error bars. Red circles denote average of all coral data per site with 2SE error bars (excluding $\delta^{234}U_{sec}$ data impacted by "vital effects"; as discussed in Section 6.2). Black shading in panel e denotes seawater samples affected by Fe-Mn oxide adsorption; these samples were excluded from the calculated mean $\delta^{238}U$ value. At all sites, corals record seawater U isotope ratios within analytical uncertainty. Across sites, subtle trends are visible, with $\delta^{238}U$ increasing and $\delta^{234}U_{sec}$ decreasing from North Atlantic to South Pacific. (For interpretation of the references to colour in this figure legend, the reader is referred to the web version of this article.)

samples. The second and third possibilities are somewhat difficult to disentangle, but prior work suggests that the third option is most likely. Specifically, fission track mapping and $\delta^{234}U_{sec}$ analyses of modern and ancient *D. dianthus* specimens (Robinson et al., 2006) have revealed preferential ^{234}U diffusion into the irregular fine-grained aragonite of the calcification centers of coral septa. As a result, closed system partitioning of $^{234}U/^{238}U$ can create intra-sample isotopic gradients. While sampling an entire coral should in theory allow the seawater $\delta^{234}U_{sec}$ value to be recovered, the magnitude of these internal gradients is sufficiently large (tens of permil) that even very subtle biases in sampling could cause a single sub-sample to contain a permil-level deficit/excess of ^{234}U, depending on which components were preferentially sampled. Thus, since the analyses here targeted large pieces of septa, but not entire septa (let alone entire corals), it is plausible that these isotopic deviations are due to the sampling of ^{234}U-poor portions

of the corals (i.e., excluding calcification centers). This inference is further supported by the distribution of $\delta^{234}U_{sec}$ values for the many sub-samples of the TN228 coral: while most samples plot near the average value of seawater at GP13 station 21, a small sub-set deviate toward lower values (Fig. 7). In the context of paleo-environmental $\delta^{234}U_{sec}$ reconstructions using deep-sea coral archives, this finding reinforces the conclusion (Robinson et al., 2006) that homogenizing large samples of entire coral septa is the best way to ensure that bulk values indeed approximate the seawater value. This approach can be further improved by sampling multiple corals from a given site and time bin, such that outliers likely to be affected by sampling bias can be identified.

In contrast to $\delta^{234}U_{sec}$, no heterogeneity is observed in the $\delta^{238}U$ data from the corals studied here (that is, all samples closely resemble ambient seawater $\delta^{238}U$ values; Figs. 6, 7, 11). This is to be expected, since the mechanisms giving rise to intra-sample

$\delta^{234}U_{sec}$ heterogeneity (progressive ^{234}U diffusion into U-poor aragonite; alpha recoil diffusion of ^{234}U) will not affect the $\delta^{238}U$ value of a sample. Coral septa therefore represent an extremely high-precision archive of seawater $\delta^{238}U$ values (to within ~0.03 ‰ for a single analysis, as discussed in Section 4.2, or to even more precise levels for replicate analyses of a given coral: avg. $\delta^{238}U$ of TN228 coral septa = -0.369 ± 0.011 ‰, avg. $\delta^{238}U$ of GP13 seawater = -0.367 ± 0.008 ‰; Fig. 7). With such a precise archive, it may be possible to observe heterogeneity in modern or ancient coral specimens across ocean basins. Indeed, our dataset shows hints of a 0.02–0.03 ‰ gradient between the North Atlantic and South Pacific sites, which is reflected in the coral data (Fig. 11), however, without more sample coverage it is difficult to further quantify the magnitude and spatial pattern of such an effect.

6.3. Impact of seawater heterogeneity on paleo-redox reconstructions

Finally, we consider the impact of spatially heterogeneous seawater and coral $\delta^{238}U$ values on paleo-redox reconstructions. A homogenous seawater $\delta^{238}U$ value is commonly assumed in paleo-redox reconstructions (see e.g., Lau et al., 2019), since samples often derive from a single locality that is used as a proxy for the global seawater composition. If a given locality is subject to the seawater $\delta^{238}U$ heterogeneity observed here (Figs. 7, 8), and that heterogeneity is recorded in biological archives such as deep-sea corals, then inferences of marine anoxia could be rendered inaccurate.

To explore the magnitude of such an effect, we utilized a recently updated U isotope mass balance framework (Kipp and Tissot, 2022). We consider two cases: a steady-state system, and a dynamic perturbation to the marine U reservoir. In each case, we first take the conservative stance that a single biological carbonate analysis cannot constrain the global seawater $\delta^{238}U$ value to better than the full range of values (−0.431 ‰ to −0.337 ‰) observed in our seawater analyses (i.e., assuming that a given carbonate archive might capture seawater anywhere on that gradient). In doing so, we see that we could not distinguish a steady state system with 0.3 % or 0.1 % fractional seafloor anoxia (f_{anox}) from the modern value (0.19 %) (Fig. 12a). This is still quite a small range compared to the anoxic extent commonly inferred during past climatic perturbations (several percent to 10's of percent; Lau et al., 2019; Kipp and Tissot, 2022), meaning that such heterogeneity does not meaningfully impact steady-state f_{anox} reconstructions for large changes in $\delta^{238}U$ mass balance. We note, however, that in past oceans with more prevalent anoxia, the shorter U residence time would imply that isotopic heterogeneities would be more pronounced; this means that global interpretations of the $\delta^{238}U$ redox proxy are compromised in strongly anoxic intervals, such as the Precambrian (X. Chen et al., 2021).

In contrast to steady-state conditions, dynamic perturbations are less well resolved, particularly if they are small in magnitude and/or occur over a short time interval. We see that on up to 240 kyr timescales, we could not resolve a decrease in f_{anox} by an order of magnitude (Fig. 12b). For increases in f_{anox}, transient increases to 1–10 % seafloor anoxia are required to exceed the variability observed in the modern ocean, depending on the duration of the perturbation (Fig. 12b).

While these calculations point to the inherent limitations of the $\delta^{238}U$ redox proxy, they are overly conservative in their threshold for "resolving" a perturbation, as we assumed analysis of a single sample from a single site, meaning we cannot resolve any spatial heterogeneity. However, if paleo-redox investigations make use of multiple sample sites (Clarkson et al., 2018, 2021; Zhang et al., 2018), then seawater heterogeneity can be accounted for, such that the reconstructions at each site are limited only by the analytical precision (at best ± 0.02 ‰ per sample). In such cases, transient
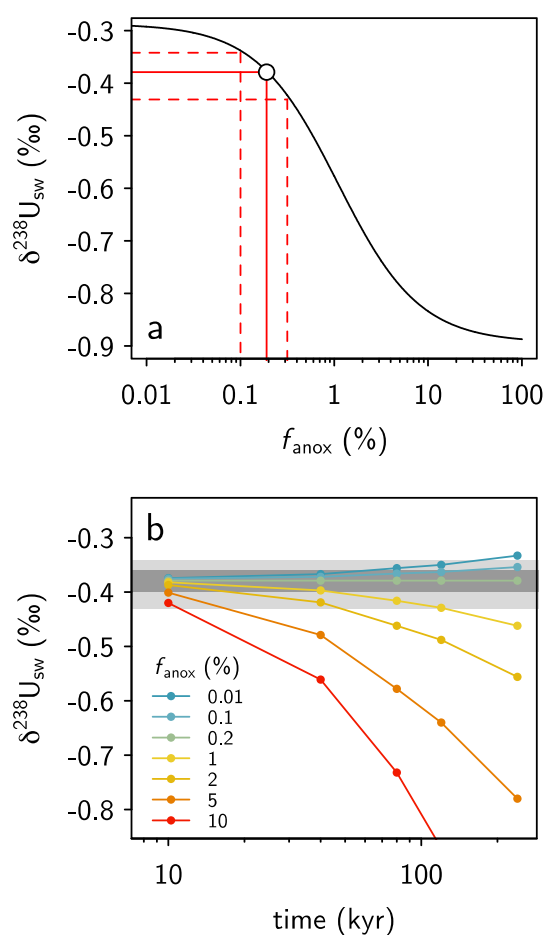
Fig. 12. Impact of heterogeneous $\delta^{238}U_{sw}$ on seafloor anoxia reconstructions for **(a)** steady-state system and **(b)** dynamic perturbation. If one measurement is used to infer $\delta^{238}U_{sw}$ of the past ocean at a given time, the upper limit on the accuracy of this inference is set by the variability in $\delta^{238}U_{sw}$ seen in the modern ocean (−0.431 ‰ to −0.337 ‰). At steady state (panel a), this corresponds to an uncertainty of 0.1 % to 0.3 % seafloor anoxia (dashed lines). In transient perturbations (panel b), this limitation is more pronounced: for short-lived (10's of kyr) perturbations, f_{anox} must reach several percent to be resolved from global ocean heterogeneity (light grey band). However, if multiple sample sites are utilized, this heterogeneity can potentially be recognized, allowing a more precise assessment of the global average $\delta^{238}U_{sw}$ value, which is ultimately limited by maximum analytical precision (±0.02 ‰; dark grey band).

increases in f_{anox} to ~1 % lasting only ~40 kyr could in theory be detected (dark grey band, Fig. 12b). While these efforts would require more complex isotope mass balance formulations than the one-box ocean typically assumed in $\delta^{238}U$ studies (Kipp and Tissot, 2022), they would have the potential to unravel subtle redox shifts with spatial information.

7. Concluding remarks

We have undertaken a systematic survey of seawater and deep-sea coral U isotope ratios at the maximum achievable precision and accuracy currently allowed by MC-ICP-MS. We find subtle isotopic heterogeneity in the ocean that results from local and/or global impacts of processes that fractionate $^{238}U/^{235}U$, as well as perhaps a small impact of mixing of heterogeneous $^{234}U/^{238}U$ reservoirs. We used these data to calculate salinity-normalized global seawater $\delta^{238}U$ (−0.379 ± 0.023 ‰) and $\delta^{234}U_{sec}$ (+145.55 ± 0.28 ‰) values. Deep sea corals (specifically *D. dianthus*) faithfully record the $\delta^{238}U$ value of ambient seawater to high precision, but their measured $\delta^{234}U_{sec}$ composition can be affected by intra-coral ^{234}U

diffusion if sampling is biased toward certain coral sub-components. In light of these findings, it is clear that optimal strategies for paleo-environmental reconstructions using such archives would best target large samples (e.g., homogenizing entire septa) and utilize multiple samples from multiple sites at a given time point in attempting to reconstruct secular trends. With such an approach, studies of U isotopes in biological archives might be able to provide precise insights into the timescales of past changes in ocean chemistry, and the extent of ancient seafloor anoxia.

Data availability

All data generated in this study are provided in the main text and supplement.

Declaration of Competing Interest

The authors declare that they have no known competing financial interests or personal relationships that could have appeared to influence the work reported in this paper.

Acknowledgements

Appendix A. Supplementary material

Supplementary material to this article can be found online at https://doi.org/10.1016/j.gca.2022.09.018.

References

Adkins, J.F., Boyle, E.A., Curry, W.B., Lutringer, A., 2003. Stable isotopes in deep-sea corals and a new mechanism for "vital effects". Geochim. Cosmochim. Acta 67, 1129–1143.

Albarède, F., Albalat, E., Télouk, P., 2015. Instrumental isotope fractionation in multiple-collector icp-ms. J. Anal. At. Spectrom. 30, 1736–1742.

Albarède, F., Telouk, P., Blichert-Toft, J., Boyet, M., Agranier, A., Nelson, B., 2004. Precise and accurate isotopic measurements using multiple-collector ICPMS. Geochim. Cosmochim. Acta 68, 2725–2744.

Anbar, A.D., Creaser, R.A., Papanastassiou, D.A., Wasserburg, G.J., 1992. Rhenium in seawater: Confirmation of generally conservative behavior. Geochim. Cosmochim. Acta 56, 4099–4103.

Andersen, M.B., Stirling, C.H., Potter, E.-K., Halliday, A.N., 2004. Toward epsilon levels of measurement precision on ^{234}U/^{238}U by using MC-ICPMS. Int. J. Mass Spectrom. 237, 107–118.

Andersen, M.B., Stirling, C.H., Porcelli, D., Halliday, A.N., Andersson, P.S., Baskaran, M., 2007. The tracing of riverine U in Arctic seawater with very precise ^{234}U/^{238}U measurements. Earth Planet. Sci. Lett. 259, 171–185.

Andersen, M.B., Stirling, C.H., Zimmermann, B., Halliday, A.N., 2010. Precise determination of the open ocean ^{234}U/^{238}U composition. Geochem. Geophys. Geosystems., 11.

Andersen, M.B., Elliott, T., Freymuth, H., Sims, K.W.W., Niu, Y., Kelley, K.A., 2015. The terrestrial uranium isotope cycle. Nature 517, 356–359.

Andersen, M.B., Romaniello, S., Vance, D., Little, S.H., Herdman, R., Lyons, T.W., 2014. A modern framework for the interpretation of ^{238}U/^{235}U in studies of ancient ocean redox. Earth Planet. Sci. Lett. 400, 184–194.

Andersen, M.B., Vance, D., Morford, J.L., Bura-Nakić, E., Breitenbach, S.F., Och, L., 2016. Closing in on the marine ^{238}U/^{235}U budget. Chem. Geol. 420, 11–22.

Andersen, M.B., Stirling, C.H., Weyer, S., 2017. Uranium isotope fractionation. Rev. Mineral. Geochem. 82, 799–850.

Andersson, P.S., Wasserburg, G.J., Chen, J.H., Papanastassiou, D.A., Ingri, J., 1995. ^{238}U–^{234}U and ^{232}Th–^{230}Th in the Baltic Sea and in river water. Earth Planet. Sci. Lett. 130, 217–234.

Avanzinelli, R., Casalini, M., Elliott, T., Conticelli, S., 2018. Carbon fluxes from subducted carbonates revealed by uranium excess at Mount Vesuvius, Italy. Geology 46, 259–262.

Bigeleisen, J., 1996. Nuclear size and shape effects in chemical reactions. Isotope chemistry of the heavy elements. J. Am. Chem. Soc. 118, 3676–3680.

Brennecka, G.A., Wadhwa, M., 2012. Uranium isotope compositions of the basaltic angrite meteorites and the chronological implications for the early Solar System. Proc. Natl. Acad. Sci. U. S. A. 109, 9299–9303.

Brennecka, G.A., Wasylenki, L.E., Bargar, J.R., Weyer, S., Anbar, A.D., 2011. Uranium isotope fractionation during adsorption to Mn-oxyhydroxides. Environ. Sci. Technol. 45, 1370–1375.

Brennecka, G.A., Budde, G., Kleine, T., 2015. Uranium isotopic composition and absolute ages of Allende chondrules. Meteorit. Planet. Sci. 50, 1995–2002.

Brennecka, G.A., Amelin, Y., Kleine, T., 2018. Uranium isotope ratios of Muonionalusta troilite and complications for the absolute age of the IVA iron meteorite core. Earth Planet. Sci. Lett. 490, 1–10.

Chabaux, F., Riotte, J., Clauer, N., France-Lanord, C., 2001. Isotopic tracing of the dissolved U fluxes of Himalayan rivers: implications for present and past U budgets of the Ganges-Brahmaputra system. Geochim. Cosmochim. Acta 65, 3201–3217.

Chabaux, F., Riotte, J., Dequincey, O., 2003. U-Th-Ra fractionation during weathering and river transport. Rev. Mineral. Geochem. 52, 533–576.

Chakrabarti, R., Mondal, S., Jacobson, A.D., Mills, M., Romaniello, S.J., Vollstaedt, H., 2021. Review of techniques, challenges, and new developments for calcium isotope ratio measurements. Chem. Geol. 581, 120398.

Chen, J.H., Edwards, R.L., Wasserburg, G.J., 1986. ^{238}U, ^{234}U and ^{232}Th in seawater. Earth Planet. Sci. Lett. 80, 241–251.

Chen, S., Littley, E.F., Rae, J.W., Charles, C.D., Adkins, J.F., 2021a. Uranium Distribution and Incorporation Mechanism in Deep-Sea Corals: Implications for Seawater [CO$_3^{2-}$] Proxies. Front. Earth Sci. 9, 159.

Chen, T., Robinson, L.F., Beasley, M.P., Claxton, L.M., Andersen, M.B., Gregoire, L.J., Wadham, J., Fornari, D.J., Harpp, K.S., 2016. Ocean mixing and ice-sheet control of seawater ^{234}U/^{238}U during the last deglaciation. Science 354, 626–629.

Chen, X., Romaniello, S.J., Herrmann, A.D., Hardisty, D., Gill, B.C., Anbar, A.D., 2018a. Diagenetic effects on uranium isotope fractionation in carbonate sediments from the Bahamas. Geochim. Cosmochim. Acta 237, 294–311.

Chen, X., Romaniello, S.J., Herrmann, A.D., Samankassou, E., Anbar, A.D., 2018b. Biological effects on uranium isotope fractionation (^{238}U/^{235}U) in primary biogenic carbonates. Geochim. Cosmochim. Acta 240, 1–10.

Chen, X., Zheng, W., Anbar, A.D., 2020. Uranium isotope fractionation (^{238}U/^{235}U) during U(VI) uptake by freshwater plankton. Environ. Sci. Technol. 54, 2744–2752.

Chen, X., Tissot, F.L.H., Jansen, M.F., Bekker, A., Liu, C.X., Nie, N.X., Halverson, G.P., Veizer, J., Dauphas, N., 2021b. The uranium isotope record of shales and carbonates through geologic time. Geochim. Cosmochim. Acta 300, 164–191.

Cheng, H., Adkins, J., Edwards, R.L., Boyle, E.A., 2000a. U-Th dating of deep-sea corals. Geochim. Cosmochim. Acta 64, 2401–2416.

Cheng, H., Edwards, R.L., Hoff, J., Gallup, C.D., Richards, D.A., Asmerom, Y., 2000b. The half-lives of uranium-234 and thorium-230. Chem. Geol. 169, 17–33.

Cheng, H., Edwards, R.L., Shen, C.-C., Polyak, V.J., Asmerom, Y., Woodhead, J., Hellstrom, J., Wang, Y., Kong, X., Spötl, C., 2013. Improvements in ^{230}Th dating, ^{230}Th and ^{234}U half-life values, and U-Th isotopic measurements by multi-collector inductively coupled plasma mass spectrometry. Earth Planet. Sci. Lett. 371, 82–91.

Chutcharavan, P.M., Dutton, A., Ellwood, M.J., 2018. Seawater ^{234}U/^{238}U recorded by modern and fossil corals. Geochim. Cosmochim. Acta 224, 1–17.

Clark, S.K., Johnson, T.M., 2008. Effective isotopic fractionation factors for solute removal by reactive sediments: A laboratory microcosm and slurry study. Environ. Sci. Technol. 42, 7850–7855.

Clarkson, M.O., Stirling, C.H., Jenkyns, H.C., Dickson, A.J., Porcelli, D., Moy, C.M., von Strandmann, P.A.P., Cooke, I.R., Lenton, T.M., 2018. Uranium isotope evidence for two episodes of deoxygenation during Oceanic Anoxic Event 2. Proc. Natl. Acad. Sci. 115, 2918–2923.

Clarkson, M.O., Lenton, T.M., Andersen, M.B., Bagard, M.-L., Dickson, A.J., Vance, D., 2021. Upper limits on the extent of seafloor anoxia during the PETM from uranium isotopes. Nat. Commun. 12, 1–9.

Craig, G., Hu, Z., Zhang, A., Lloyd, N.S., Bouman, C., Schwieters, J., 2017. Dynamic time correction for high precision isotope ratio measurements. Thermo Fish Sci Brem., 1–8.

Dahl, T.W., Connelly, J.N., Li, D., Kouchinsky, A., Gill, B.C., Porter, S., Maloof, A.C., Bizzarro, M., 2019. Atmosphere-ocean oxygen and productivity dynamics during early animal radiations. Proc. Natl. Acad. Sci. U. S. A. 116, 19352–19361.

Dahl, T.W., Boyle, R.A., Canfield, D.E., Connelly, J.N., Gill, B.C., Lenton, T.M., Bizzarro, M., 2014. Uranium isotopes distinguish two geochemically distinct stages during the later Cambrian SPICE event. Earth Planet. Sci. Lett. 401, 313–326.

Dahl, T.W., Connelly, J.N., Kouchinsky, A., Gill, B.C., Månsson, S.F., Bizzarro, M., 2017. Reorganisation of Earth's biogeochemical cycles briefly oxygenated the oceans 520 Myr ago. Geochem. Perspect. Lett. 10, 210–220.

Dang, D.H., Novotnik, B., Wang, W., Bastian, G.R., Douglas, E.R., 2016. Uranium isotope fractionation during adsorption, (co)precipitation, and biotic reduction. Environ. Sci. Technol. 50, 12695–12704.

Dang, D.H., Evans, R.D., Wang, W., Omanović, D., El Houssainy, A., Lenoble, V., Mullot, J.U., Mounier, S., Garnier, C., 2018. Uranium isotope geochemistry in modern coastal sediments: Insights from Toulon Bay, France. Chem. Geol. 481, 133–145.

Dang, D.H., Wang, W., Gibson, T.M., Kunzmann, M., Andersen, M.B., Halverson, G.P., Evans, R.D., 2022. Authigenic uranium isotopes of late Proterozoic black shale. Chem. Geol. 588, 120644.

Dauphas, N., Pourmand, A., Teng, F.-Z., 2009. Routine isotopic analysis of iron by HR-MC-ICPMS: How precise and how accurate?. Chem. Geol. 267, 175–184.

Dickson, A.J., Hsieh, Y.-T., Bryan, A., 2020. The rhenium isotope composition of Atlantic Ocean seawater. Geochim. Cosmochim. Acta 287, 221–228.

Dodson, M.H., 1963. A theoretical study of the use of internal standards for precise isotopic analysis by the surface ionization technique: Part I-General first-order algebraic solutions. J. Sci. Instrum. 40, 289.

Dunk, R.M., Mills, R.A., Jenkins, W.J., 2002. A reevaluation of the oceanic uranium budget for the Holocene. Chem. Geol. 190, 45–67.

Edwards, R.L., Chen, J.H., Ku, T.-L., Wasserburg, G.J., 1987a. Precise timing of the last interglacial period from mass spectrometric determination of thorium-230 in corals. Science 236, 1547–1553.

Edwards, R.L., Chen, J.H., Wasserburg, G.J., 1987b. ^{238}U–^{234}U–^{230}Th–^{232}Th systematics and the precise measurement of time over the past 500,000 years. Earth Planet. Sci. Lett. 81, 175–192.

Ellwood, M.J., Bowie, A.R., Baker, A., Gault-Ringold, M., Hassler, C., Law, C.S., Maher, W.A., Mariner, A., Nodder, S., Sander, S., Stevens, C., Townsend, A., van der Merwe, P., Woodward, E.M.S., Wuttig, K., Boyd, P., 2018. Insights into the biogeochemical cycling of iron, nitrate, and phosphate across a 5,300 km South Pacific zonal section (153°E-150°W). Global Biogeochem Cy 32, 187–207.

Freymuth, H., Andersen, M.B., Elliott, T., 2019. Uranium isotope fractionation during slab dehydration beneath the Izu arc. Earth Planet. Sci. Lett. 522, 244–254.

Gagnon, A.C., Adkins, J.F., Fernandez, D.P., Robinson, L.F., 2007. Sr/Ca and Mg/Ca vital effects correlated with skeletal architecture in a scleractinian deep-sea coral and the role of Rayleigh fractionation. Earth Planet. Sci. Lett. 261, 280–295.

Goldmann, A., Brennecka, G., Noordmann, J., Weyer, S., Wadhwa, M., 2015. The uranium isotopic composition of the Earth and the Solar System. Geochim. Cosmochim. Acta 148, 145–158.

Gothmann, A.M., Higgins, J.A., Adkins, J.F., Broecker, W., Farley, K.A., McKeon, R., Stolarski, J., Planavsky, N., Wang, X., Bender, M.L., 2019. A Cenozoic record of seawater uranium in fossil corals. Geochim. Cosmochim. Acta 250, 173–190.

Goto, K.T., Anbar, A.D., Gordon, G.W., Romaniello, S.J., Shimoda, G., Takaya, Y., Tokumaru, A., Nozaki, T., Suzuki, K., Machida, S., 2014. Uranium isotope systematics of ferromanganese crusts in the Pacific Ocean: Implications for the marine ^{238}U/^{235}U isotope system. Geochim. Cosmochim. Acta 146, 43–58.

Halliday, A.N., Lee, D.-C., Christensen, J.N., Rehkämper, M., Yi, W., Luo, X., Hall, C.M., Ballentine, C.J., Pettke, T., Stirling, C., 1998. Applications of multiple collector-ICPMS to cosmochemistry, geochemistry, and paleoceanography. Geochim. Cosmochim. Acta 62, 919–940.

Hart, S.R., Zindler, A., 1989. Isotope fractionation laws: a test using calcium. Int. J. Mass Spectrom. Ion Process. 89, 287–301.

Henderson, G.M., 2002. Seawater (^{234}U/^{238}U) during the last 800 thousand years. Earth Planet. Sci. Lett. 199, 97–110.

Hines, S.K.V., Southon, S.R., Adkins, J.F., 2015. A high-resolution record of Southern Ocean intermediate water radiocarbon over the past 30,000 years. Earth Planet. Sci. Lett. 432, 46–58.

Holmden, C., Amini, M., Francois, R., 2015. Uranium isotope fractionation in Saanich Inlet: A modern analog study of a paleoredox tracer. Geochim. Cosmochim. Acta 153, 202–215.

Iizuka, T., Amelin, Y., Kaltenbach, A., Koefoed, P., Stirling, C.H., 2014. U-Pb systematics of the unique achondrite Ibitira: Precise age determination and petrogenetic implications. Geochim. Cosmochim. Acta 132, 259–273.

John, S.G., Adkins, J.F., 2010. Analysis of dissolved iron isotopes in seawater. Mar. Chem. 119, 65–76.

Kimura, J.-I., Chang, Q., Kanazawa, N., Sasaki, S., Vaglarov, B.S., 2016. High-precision in situ analysis of Pb isotopes in glasses using 10^{13} Ω resistor high gain amplifiers with ultraviolet femtosecond laser ablation multiple Faraday collector inductively coupled plasma mass spectrometry. J. Anal. At. Spectrom. 31, 790–800.

Kipp, M.A., Tissot, F.L., 2022. Inverse methods for consistent quantification of seafloor anoxia using uranium isotope data from marine sediments. Earth Planet. Sci. Lett. 577, 117240.

Klaver, M., Smeets, R.J., Koornneef, J.M., Davies, G.R., Vroon, P.Z., 2016. Pb isotope analysis of ng size samples by TIMS equipped with a 10^{13} Ω resistor using a ^{207}Pb–^{204}Pb double spike. J. Anal. At. Spectrom. 31, 171–178.

Klinkhammer, G.P., Palmer, M.R., 1991. Uranium in the oceans: Where it goes and why. Geochim. Cosmochim. Acta 55, 1799–1806.

Ku, T.-L., 1965. An evaluation of the U^{234}/U^{238} method as a tool for dating pelagic sediments. J. Geophys. Res. 70, 3457–3474.

Ku, T.-L., Knauss, K.G., Mathieu, G.G., 1977. Uranium in open ocean: concentration and isotopic composition. Deep Sea Res. 24, 1005–1017.

Lau, K.V., Macdonald, F.A., Maher, K., Payne, J.L., 2017. Uranium isotope evidence for temporary ocean oxygenation in the aftermath of the Sturtian Snowball Earth. Earth Planet. Sci. Lett. 458, 282–292.

Lau, K.V., Maher, K., Altiner, D., Kelley, B.M., Kump, L.R., Lehrmann, D.J., Silva-Tamayo, J.C., Weaver, K.L., Yu, M., Payne, J.L., 2016. Marine anoxia and delayed Earth system recovery after the end-Permian extinction. Proc. Natl. Acad. Sci. U. S. A. 113, 2360–2365.

Lau, K.V., Romaniello, S.J., Zhang, F., 2019. The uranium isotope paleoredox proxy. Cambridge University Press.

Lau, K.V., Lyons, T.W., Maher, K., 2020. Uranium reduction and isotopic fractionation in reducing sediments: Insights from reactive transport modeling. Geochim. Cosmochim. Acta 287, 65–92.

Livermore, B.D., Dahl, T.W., Bizzarro, M., Connelly, J.N., 2020. Uranium isotope compositions of biogenic carbonates - Implications for U uptake in shells and the application of the paleo-ocean oxygenation proxy. Geochim. Cosmochim. Acta 287, 50–64.

Maréchal, C.N., Télouk, P., Albarède, F., 1999. Precise analysis of copper and zinc isotopic compositions by plasma-source mass spectrometry. Chem. Geol. 156, 251–273.

Menzel Barraqueta, J.-L., Klar, J.K., Gledhill, M., Schlosser, C., Shelley, R., Planquette, H.F., Wenzel, B., Sarthou, G., Achterberg, E.P., 2019. Atmospheric deposition fluxes over the Atlantic Ocean: a GEOTRACES case study. Biogeosciences 16, 1525–1542.

Merle, R., Amelin, Y., Yin, Q.Z., Huyskens, M.H., Sanborn, M.E., Nagashima, K., Yamashita, K., Ireland, T.R., Krot, A.N., Sieber, M.J., 2020. Exploring the efficiency of stepwise dissolution in removal of stubborn non-radiogenic Pb in chondrule U-Pb dating. Geochim. Cosmochim. Acta 277, 1–20.

Morford, J.L., Emerson, S., 1999. The geochemistry of redox sensitive trace metals in sediments. Geochim. Cosmochim. Acta 63, 1735–1750.

Murphy, M.J., Stirling, C.H., Kaltenbach, A., Turner, S.P., Schaefer, B.F., 2014. Fractionation of 238U/235U by reduction during low temperature uranium mineralisation processes. Earth Planet. Sci. Lett. 388, 306–317.

Nguyen, H.D., Riley, M., Leys, J., Salter, D., 2019. Dust storm event of February 2019 in central and east coast of Australia and evidence of long-range transport to New Zealand and Antarctica. Atmosphere 10, 653.

Nier, A.O., 1939. The isotopic constitution of uranium and the half-lives of the uranium isotopes. I.. Phys. Rev. 55, 150.

Owens, S.A., Buesseler, K.O., Sims, K.W.W., 2011. Re-evaluating the ^{238}U-salinity relationship in seawater: Implications for the ^{238}U–^{234}Th disequilibrium method. Mar. Chem. 127, 31–39.

Richter, S., Eykens, R., Kuhn, H., Aregbe, Y., Verbruggen, A., Weyer, S., 2010. New average values for the n(^{238}U)/n(^{235}U) isotope ratios of natural uranium standards. Int. J. Mass Spectrom. 295, 94–97.

Richter, S., Goldberg, S.A., Mason, P.B., Traina, A.J., Schwieters, J.B., 2001. Linearity tests for secondary electron multipliers used in isotope ratio mass spectrometry. Int. J. Mass Spectrom. 206, 105–127.

Robinson, L.F., Belshaw, N.S., Henderson, G.M., 2004a. U and Th concentrations and isotope ratios in modern carbonates and waters from the Bahamas. Geochim. Cosmochim. Acta 68, 1777–1789.

Robinson, L.F., Henderson, G.M., Hall, L., Matthews, I., 2004b. Climatic control of riverine and seawater uranium-isotope ratios. Science 305, 851–854.

Robinson, L.F., Adkins, J.F., Keigwin, L.D., Southon, J., Fernandez, D.P., Wang, S.L., Scheirer, D.S., 2005. Radiocarbon variability in the western North Atlantic during the last deglaciation. Science 310, 1469–1473.

Robinson, L.F., Adkins, J.F., Fernandez, D.P., Burnett, D.S., Wang, S.-L., Gagnon, A.C., Krakauer, N., 2006. Primary U distribution in scleractinian corals and its implications for U series dating. Geochem. Geophys. Geosystems, 7.

Robinson, L.F., Adkins, J.F., Scheirer, D.S., Fernandez, D.P., Gagnon, A., Waller, R.G., 2007. Deep-sea scleractinian coral age and depth distributions in the northwest Atlantic for the last 225,000 years. Bull. Mar. Sci. 81, 371–391.

Rolison, J.M., Stirling, C.H., Middag, R., Rijkenberg, M.J., 2017. Uranium stable isotope fractionation in the Black Sea: Modern calibration of the ^{238}U/^{235}U paleo-redox proxy. Geochim. Cosmochim. Acta 203, 69–88.

Romaniello, S.J., Herrmann, A.D., Anbar, A.D., 2013. Uranium concentrations and ^{238}U/^{235}U isotope ratios in modern carbonates from the Bahamas: Assessing a novel paleoredox proxy. Geochim. Cosmochim. Acta 362, 305–316.

Russell, W.A., Papanastassiou, D.A., Tombrello, T.A., 1978. Ca isotope fractionation on the Earth and other solar system materials. Geochim. Cosmochim. Acta 42, 1075–1090.

Schlitzer, R., Anderson, R.F., Dodas, E.M., Lohan, M., Geibert, W., Tagliabue, A., Bowie, A., Jeandel, C., Maldonado, M.T., Landing, W.M., 2018. The GEOTRACES intermediate data product 2017. Chem. Geol. 493, 210–223.

Stichel, T., Kretschmer, S., Geibert, W., Lambelet, M., Plancherel, Y., Rutgers van der Loeff, M., van de Flierdt, T., 2020. Particle–seawater interaction of neodymium in the North Atlantic. ACS Earth Space Chem. 4, 1700–1717.

Stirling, C.H., Esat, T.M., McCulloch, M.T., Lambeck, K., 1995. High-precision U-series dating of corals from Western Australia and implications for the timing and duration of the Last Interglacial. Earth Planet. Sci. Lett. 135, 115–130.

Stirling, C.H., Andersen, M.B., Potter, E.-K., Halliday, A.N., 2007. Low-temperature isotopic fractionation of uranium. Earth Planet. Sci. Lett. 264, 208–225.

Thiagarajan, N., Gerlach, D., Roberts, M.L., Burke, A., McNichol, A., Jenkins, W.J., Subhas, A.V., Thresher, R.E., Adkins, J.F., 2013. Movement of deep-sea coral populations on climatic timescales. Paleoceanogr. Paleoclimatol. 28, 227–236.

Tissot, F.L.H., Dauphas, N., Grossman, L., 2016. Origin of uranium isotope variations in early solar nebula condensates. Sci. Adv. 2, e1501400.

Tissot, F.L.H., Chen, C., Go, B., Naziemiec, M., Healy, G., Bekker, A., Swart, P.K., Dauphas, N., 2018. Controls of eustasy and diagenesis on the ^{238}U/^{235}U of carbonates and evolution of the seawater (^{234}U/^{238}U) during the last 1.4 Myr. Geochim. Cosmochim. Acta. 242, 233–265.

Tissot, F.L., Dauphas, N., 2015. Uranium isotopic compositions of the crust and ocean: Age corrections, U budget and global extent of modern anoxia. Geochim. Cosmochim. Acta 167, 113–143.

Tissot, F.L., Ibañez-Mejia, M., 2021. Unlocking the Single-Crystal Record of Heavy Stable Isotopes. Elem. Int. Mag. Mineral. Geochem. Petrol. 17, 389–394.

Tissot, F.L., Ibanez-Mejia, M., Boehnke, P., Dauphas, N., McGee, D., Grove, T.L., Harrison, T.M., 2019. ^{238}U/^{235}U measurement in single-zircon crystals: implications for the Hadean environment, magmatic differentiation and geochronology. J. Anal. At. Spectrom. 34, 2035–2052.

Veeh, H.H., 1967. Deposition of uranium from the ocean. Earth Planet. Sci. Lett. 3, 145–150.

Verbruggen, A., Alonso, A., Eykens, R., Kehoe, F., Kuhn, H., Richter, S., Aregbe, Y., 2008 Preparation and certification of IRMM-3636, IRMM-3636a and IRMM-3636b.

Wang, X., Planavsky, N.J., Reinhard, C.T., Hein, J.R., Johnson, T.M., 2016. A Cenozoic seawater redox record derived from ^{238}U/^{235}U in ferromanganese crusts. Am. J. Sci. 316, 64–83.

Wang, X., Planavsky, N.J., Hofmann, A., Saupe, E.E., De Corte, B.P., Philippot, P., LaLonde, S.V., Jemison, N.E., Zou, H., Ossa, F.O., Rybacki, K., Alfimova, N., Larson, M.J., Tsikos, H., Fralick, P.W., Johnson, T.M., Knudsen, A.C., Reinhard, C.T., Konhauser, K.O., 2018. A Mesoarchean shift in uranium isotope systematics. Geochim. Cosmochim. Acta 238, 438–452.

Wang, X.T., Sigman, D.M., Prokopenko, M.G., Adkins, J.F., Robinson, L.F., Hines, S.K., Chai, J., Studer, A.S., Martinez-Garcia, A., Chen, T., 2017. Deep-sea coral evidence for lower Southern Ocean surface nitrate concentrations during the last ice age. Proc. Natl. Acad. Sci. U. S. A. 114, 3352–3357.

Wasserburg, G.J., Papanastassiou, D.A., Nenow, E.V., Bauman, C.A., 1969. A programmable magnetic field mass spectrometer with on-line data processing. Rev. Sci. Instrum. 40, 288–295.

Wendt, I., Carl, C., 1991. The statistical distribution of the mean squared weighted deviation. Chem. Geol. Isot. Geosci. Sect. 86, 275–285.

Weyer, S., Anbar, A.D., Gerdes, A., Gordon, G.W., Algeo, T.J., Boyle, E.A., 2008. Natural fractionation of $^{238}U/^{235}U$. Geochim. Cosmochim. Acta 72, 345–359.

Wombacher, F., Rehkämper, M., 2003. Investigation of the mass discrimination of multiple collector ICP-MS using neodymium isotopes and the generalised power law. J. Anal. At. Spectrom. 18, 1371–1375.

Zhang, F., Algeo, T.J., Romaniello, S.J., Cui, Y., Zhao, L., Chen, Z.-Q., Anbar, A.D., 2018. Congruent Permian-Triassic $\delta^{238}U$ records at Panthalassic and Tethyan sites: Confirmation of global-oceanic anoxia and validation of the U-isotope paleoredox proxy. Geology 46, 327–330.